Heliyon 10 (2024) e26662

Contents lists available at ScienceDirect

Heliyon

journal homepage: www.cell.com/heliyon

Research article

In situ synthesis of long tubular water-dispersible polyaniline with core/shell gold and silver@graphene oxide nanoparticles for gas sensor application

Zahra babaei [a], Bahareh Rezaei [b], Ehsan Gholami [c], Faramarz Afshar Taromi [a,*], Amir Hossein Haghighi [d,**]

[a] Department of Polymer Engineering, Amirkabir University of Technology, Tehran, Iran
[b] Department of Chemistry, Amirkabir University of Technology, Tehran, Iran
[c] Department of Engineering, Persian Gulf University, Bushehr, Iran
[d] Department of Polymer Engineering, Shiraz Branch, Islamic Azad University, Shiraz, Iran

ARTICLE INFO

Keywords:
Polyaniline
Gold and silver nanoparticles
Graphene oxide
Tubular structure
Core/shell
Gas sensor

ABSTRACT

Gold nanoparticles (Au NPs) with graphene oxide (GO) shell (Au@GO), silver nanoparticles (Ag NPs) with GO shell (Ag@GO), and gold silver nanoparticles (AuAgNPs) with GO shell (AuAg@GO) were synthesized employing a cationic surfactant. The prepared core@shell structures were used for in situ synthesis of long tubular polyaniline structures employing cetyl trimethyl ammonium bromide (CTAB) as a soft template. This process led to a notable enhancement in the tubular nanostructure of PANI, extending its length beyond 10 μm, in the case of using core/shell Au@GO, Ag@GO, and AuAg@GO structures. To evaluate their applicability and compatibility, the dispersibility of these nanocomposites was assessed in three distinct solvents: water, dimethyl sulfoxide (DMSO), and N-Methyl-2-pyrrolidone (NMP). Subsequently, the dedoping of PANI within the prepared nanocomposites was scrutinized using UV–Visible (UV–Vis) spectroscopy, which revealed a reduction in the I_{750}/I_{315} ratio from 1.00 to 0.66 when subjected to water and NMP solvents, respectively. Notably, the dedoping of the AuAg@GO/PANI nanocomposite was predominantly observed in NMP, attributable to the presence of hydrogen bonding interactions and the basic properties of NMP. In terms of ionic conductivity, it was observed that the prepared nanocomposite exhibited its highest conductivity in a water-based medium, registering at 1982 μs. Furthermore, the AuAg@GO/PANI nanocomposite exhibited superior sensing capabilities in comparison to PANI-based gas sensor devices, particularly when exposed to acetone, CO_2, NO_2, and H_2S. Remarkably, at room temperature (25 °C), the AuAg@GO/PANI nanocomposite displayed rapid response and recovery times, with values of 279 s, 431 s, 335 s, and 509 s for 1 ppm concentrations of CO_2, NO_2, H_2S, and acetone, respectively. The sensitivity of these sensors towards acetone, CO_2, NO_2, and H_2S, was quantified by analyzing the slope of the response versus the target gas concentration, revealing the AuAg@GO/PANI nanocomposite to exhibit the highest sensitivity, particularly towards NO_2.

* Corresponding author.
** Corresponding author.
E-mail addresses: afshar@aut.ac.ir (F. Afshar Taromi), haghighi.amirhossein@iau.ac.ir, haghighi.ah@gmail.com (A.H. Haghighi).

https://doi.org/10.1016/j.heliyon.2024.e26662
Received 4 August 2023; Received in revised form 8 February 2024; Accepted 16 February 2024
Available online 18 February 2024

1. Introduction

Monitoring gases, especially toxic ones, is of paramount importance across various domains such as agriculture, automotive, security, aviation, healthcare, environmental monitoring, and industry [1,2]. To address this need, a wide range of sensors based on both organic conductive polymers and inorganic metal oxides has been extensively explored [3]. Among these, chemical gas sensors utilizing conducting polymers like polypyrrole (PPy), polyaniline (PANI), poly (3,4-ethylene-dioxythiophene) (PEDOT), and polythiophene (P3HT) have garnered attention due to their cost-effectiveness, lightweight nature, flexibility, facile synthesis processes, and the ability to operate at room temperature [4,5]. Notably, polyaniline (PANI) stands out as one of the most promising conductive materials, capable of transitioning between various oxidation states, including non-conductive, fully oxidized, and reduced forms, such as pernigraniline, and the conducting emeraldine salt, which can be achieved through slight doping [6]. PANI's simplicity of synthesis, inherent self-doping characteristics, and high solubility in alkaline solutions render it particularly attractive for industrial applications and sensor development [6]. However, despite its merits, PANI has faced challenges related to high response times, low sensitivity, inadequate stability, susceptibility to humidity, and incomplete reversibility of sensor responses [7]. In response to these limitations, researchers have explored various strategies and materials, including PANI nanostructures and PANI nanocomposites.

Studies have demonstrated the synthesis of PANI nanostructures at the nanoscale through both soft [8–12] and hard templates [13–16]. In the hard template method, diverse types of hard templates, such as porous templates [15] and zeolite channel [16], have been introduced by researchers. However, employing hard templates necessitates complex post-treatment procedures for PANI extraction, which can potentially damage the PANI structure. Therefore, soft templates, including micelles [11], vesicles [8], PANI oligomers [9,10], carbon nanotubes (CNT) [17], biological molecules like vitamin C [18], reactive oxide templates [19], and emulsifiers [20], have gained preference due to their controllable properties. Research findings indicate that the utilization of PANI in nanoparticle, nanofiber, nanowire, and nanotube forms has been proposed to enhance sensor response times by increasing the surface-to-volume ratio [21,22]. Furthermore, PANI nanocomposites, combining the advantages of both inorganic materials and PANI, have exhibited remarkable responses to gases such as hydrogen sulfide (H_2S), ammonia (NH_3), hydrogen (H_2), nitrogen dioxide (NO_2), hydrochloric acid (HCl), sulfur dioxide (SO_2), carbon monoxide (CO), carbon dioxide (CO_2), and other volatile organic compounds (VOCs) [23–25]. Essentially, the incorporation of metallic nanoparticles (NPs) into PANI has enhanced gas sensor performance through two mechanisms. First, n-type semi-conductive nanoparticles introduced into PANI can create depletion regions with reduced conductivity at PANI/nanoparticle interfaces, thereby widening the depletion region can enhance sensor response [26]. Second, the application of inorganic nanostructures like gold (Au), silver (Ag), palladium (Pd), and copper (Cu) facilitates gas adsorption on the nanostructure surface due to their catalytic properties [27]. For instance, Kinyanjui et al. introduced a novel approach for PANI-gold nanoparticle (Au NPs) synthesis, where they demonstrated that $HAuCl_4$ could serve as both a metal salt and an oxidizing agent. In this process, the synthesized gold nanoparticles exhibited uniform dispersion within the PANI matrix. However, due to the amorphous structure of PANI, the surface area of the resulting PANI-gold nanoparticles was limited [28]. Iole Venditti et al. employed an Au/PANI nanocomposite for the detection of H_2O and NH_3, achieving a 1.9% ppm^{-1} improvement in response compared to PANI alone [29]. Researchers have also explored graphene oxide (GO) combined with PANI, observing conductivity and capacitance dependencies on the PANI/GO nanocomposite microstructure when using varying ratios of cetyl trimethyl ammonium bromide (CTAB)-stabilized GO [30]. Graphene oxide, known for its 2D structure and advantageous properties such as ease of fabrication, cost-effectiveness, rapid processability, facile functionalization through oxidation, and a large surface area ($2.6 \times 103\ m^2/g$), holds significant promise for gas sensor applications [31,32]. Furthermore, researches used activated charcoal/PANI composite for selective sensing of methanol vapor [33]. Polyaniline montmorillonite reduce graphene oxide polymer nanocomposite material was also used for detection of hydrogen cyanide gas [34]. Montmorillonite-reduced graphene oxide combination enhances the material's structural and electrical properties. In gas sensing applications, MRGO demonstrates improved sensitivity and selectivity due to its increased surface area and the synergistic effects between graphene and montmorillonite. Researchers also used Ag-decorated ZnO nanorods/PANI nanocomposite for detecting Ammonia gas [35]. A gas sensing response of 59% for 120 ppm NH_3 gas was achieved with a 10 % loading of ZnO, and further enhancement was demonstrated by embedding Ag-decorated ZnO nanorods in the PANi matrix, resulting in a highly selective and sensitive sensor with a chemiresistive response of 70% at 120 ppm NH_3 and a recovery time of less than 120 s at room temperature.

In this article, we introduce a novel architecture featuring long tubular PANI nanocomposites, using an AuAg@GO core/shell structure and CTAB as the soft cationic surfactant. Our study explores the impact of CTAB concentration on the tubular structure of PANI in the presence of the AuAg@GO nanocomposite. We also investigate the effects of different solvents (water, dimethyl sulfoxide (DMSO), N-Methyl-2-pyrrolidone (NMP)) on conductivity, solubility, and de-doping of the nanocomposites. To the best of our knowledge, no prior scientific reports have detailed the in-situ synthesis of AuAg@GO and PANI with a controllable polymer shape, utilizing CTAB as a soft template. Furthermore, the synthesized AuAg@GO/PANI nanocomposite is assessed as a gas sensor for the detection of acetone, CO_2, NO_2, and H_2S, revealing significant reductions in response time and recovery time. The proposed PANI nanocomposite architecture holds promise for applications in sensors, catalysis, energy storage, and optoelectronic devices.

2. Experimental section

2.1. Materials

Ammonium persulfate (APS), silver nitrate ($AgNO_3$), sodium borohydride ($NaBH_4$) and cetyl trimethyl ammonium bromide (CTAB) were purchased from Sigma-Aldrich and were used as received. Chloroauric acid ($HAuCl_4$), trisodium citrate (TSC), aniline, and graphite powder were acquired from Merck and used as received without any purification. All the solvents were also obtained from

Merck and deionized water was used for the synthesis throughout the experiment.

2.2. Synthesis of gold and silver nanoparticles

Silver nanoparticles were synthesized using chemical reduction of $AgNO_3$ with $NaBH_4$ as reducing and stabilizing agent [36] [Fig. S1]. Gold nanoparticles were synthesized using turkevich method [37][Fig. S2]. The detailed process of synthesizing silver NPs and gold NPs are illustrated in the supporting information.

2.3. Synthesis of core/shell Au@GO and Ag@GO nanostructure

CTAB powder was dissolved in deionized (DI) water (15 mM) and stirred for 6 h, so that no bubbles were left. 4 mL of Au NPs solution (10^{-13} M) was added to 4 mL of prepared CTAB solution and stirred for 30 min until micelles were formed on the outer layer of nanoparticles. Therefore, negative zeta potential of Au NPs due to TSC changed to positive because of CTAB micellar structure (not shown here). Filtered graphene oxide (2 mL, 1 mg/mL) was added dropwise to the solution (Fig. S3). The detailed process of synthesizing GO is illustrated in the supporting information. Core/shell structure of Au@GO was prepared in this way and stored at 8 °C for further experiments (Fig. S4) [38]. The same procedure was applied for the preparation of Ag@GO nanostructure (Fig. S5).

2.4. Synthesis of long tubular Au@GO/PANI, Ag@GO/PANI and AuAg@GO/PANI nanocomposites

To study the impact of soft template concentration on PANI nanostructure, CTAB was added, without any core/shell nanocomposite, in portions of 5, 10, 15, 20 and 25 mL. In this procedure, CTAB solutions were added to 0.2 mL of aniline and HCl (10 mL, 1 N) and stirred for 15 min. APS (0.6 g) was dissolved in 10 mL HCl (1 N) and stirred for 5 min. APS solution was added dropwise to the prepared monomer/CTAB/HCl solution at 0 °C and was stirred for 24 h. In accordance with the PANI nanostructure, 10 mL CTAB was chosen as the optimum amount for the rest of experiments.

For the synthesis of Au@GO/PANI, Ag@GO/PANI, and AuAg@GO/PANI nanocomposites the same procedure was applied. In the first step of polymerization, however, 10 mL CTAB was also added to the NPs@GO solutions. 10 mL CTAB and 10, 20, and 30 mL of core/shell solutions of Au@GO and Ag@GO were added separately to the monomer/HCl mixture followed by dropwise addition of the APS solution for the synthesis of Au@GO/PANI and Ag@GO/PANI nanocomposites. AuAg@GO/PANI nanocomposite was prepared by adding 10, 15, and 20 mL of each of the Au@GO/PANI and Ag@GO/PANI solutions to the monomer/HCl mixture followed by dropwise addition of the APS solution. These were named Au_{10}@GO/PANI, Au_{20}@GO/PANI and Au_{30}@GO/PANI for Au nanocomposites, Ag_{10}@GO/PANI, Ag_{20}@GO/PANI and Ag_{30}@GO/PANI for Ag nanocomposites and $Au_{10}Ag_{10}$@GO/PANI, $Au_{15}Ag_{15}$@GO/PANI and $Au_{20}Ag_{20}$@GO/PANI for Au and Ag nanocomposites. Table 1 illustrates compositions of synthesized nanocomposites. The mixtures were stirred overnight at 0 °C the color changed from yellow to light red then purple, blue and green, consecutively. This procedure is illustrated in Scheme 1.

To compare structural impact of the soft template, the same procedure was adopted for PANI synthesis, this time without introducing any CTAB and core/shell solutions.

2.5. Characterization methods

In this experiment, Fourier transform infrared spectroscopy (FTIR), UV–Vis spectroscopy (UV–Vis), X-ray diffraction (XRD) analysis were performed to characterize prepared nanocomposites. FTIR analysis was carried out using Bomem (Hartmann & Braun) with accelerating voltage of 230 V. XRD patterns were acquired from EQUINOX3000 Intel (Cu Kα, $\lambda = 0.15418$ nm, 40 kV, 30 mA). UV–Vis was performed using Specord 210 Analytik jena (220–240 V). Field emission scanning electron microscopy (FESEM), energy-dispersive X-ray spectroscopy and elemental map were performed using KYKY-EM3200 with the resolution of 6.0 nm and accelerating voltage of 30 kV to study Au@GO/PANI and Ag@GO/PANI nanostructures. Ionic conductivity was measured using 4510 Jenway conductivity meter in solution. Thermogravimetric analysis (TGA) was performed using Mettler Toledo instrument in the range of 25–800 °C. Transmission electron microscopy (TEM) was performed using Philips FM208S 100Kv instrument.

Table 1
Compositions of synthesized nanocomposites.

Sample name	CTAB (mL) (15 mM)	Au@GO solution (10^{-13} M)	Ag@GO solution (10^{-13} M)	Aniline solution in HCl (mL)
Au_{10}@GO/PANI	10	10	–	10
Au_{20}@GO/PANI	10	20	–	10
Au_{30}@GO/PANI	10	30	–	10
Ag_{10}@GO/PANI	10	–	10	10
Ag_{20}@GO/PANI	10	–	20	10
Ag_{30}@GO/PANI	10	–	30	10
$Au_{10}Ag_{10}$@GO/PANI	10	10	10	10
$Au_{15}Ag_{15}$@GO/PANI	10	15	15	10
$Au_{20}Ag_{20}$@GO/PANI	10	20	20	10

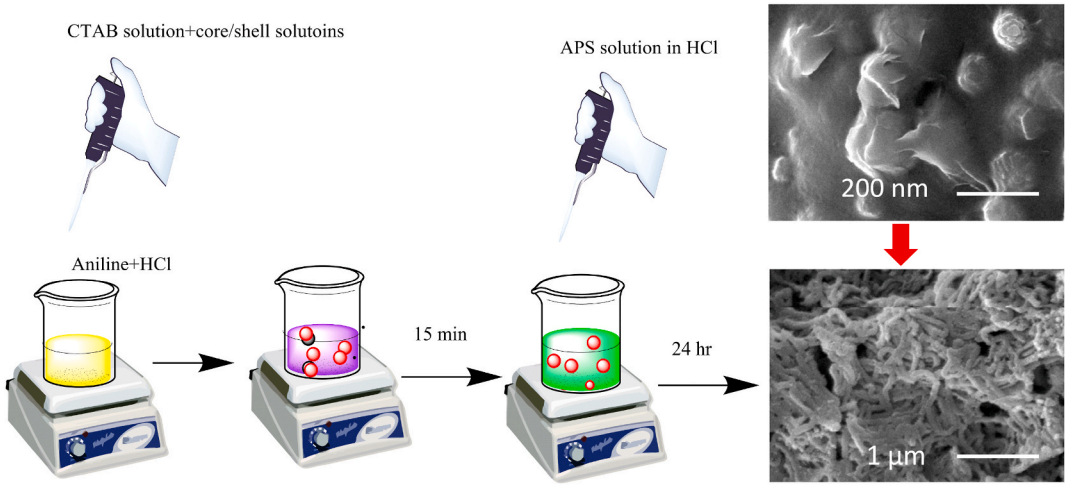

Scheme 1. Synthesis procedure of metal NPs@GO/PANI nanocomposite.

3. Result and discussion

3.1. Au@GO/PANI, Ag@GO/PANI and AuAg@GO/PANI characterization

Nine samples of Au_{10}@GO/PANI, Au_{15}@GO/PANI, Au_{20}@GO/PANI, Ag_{10}@GO/PANI, Ag_{15}@GO/PANI, Ag_{20}@GO/PANI, $Au_{10}Ag_{10}$@GO/PANI, $Au_{15}Ag_{15}$@GO/PANI, and $Au_{20}Ag_{20}$@GO/PANI underwent analysis using a four-point probe, with the resulting data revealing that the nanocomposites Au_{20}@GO/PANI, Ag_{10}@GO/PANI, and $Au_{15}Ag_{15}$@GO/PANI exhibited the highest levels of conductivity (Table S1). Consequently, these particular samples were chosen for subsequent procedures.

The molecular structures of PANI, Au_{20}@GO/PANI, Ag_{10}@GO/PANI, and $Au_{15}Ag_{15}$@GO/PANI were characterized through Fourier transform infrared spectroscopy (FTIR), as depicted in Fig. 1. Notably, the FTIR analysis revealed the presence of specific vibrational modes within the polymers. The C═C stretching vibrations of the quinoid ring and the C═C stretching vibrations of benzenoid rings of PANI appeared at approximately 1587 cm^{-1} and 1498 cm^{-1}, respectively. These characteristic peaks provide evidence of amine and imine nitrogen units within the polymer's backbone. Furthermore, the observation of in-plane and out-of-plane C–H bending in the aromatics of the 1,4-aromatic ring at 1132 cm^{-1} and 824 cm^{-1}, respectively, indicated a linear PANI structure [39]. Additional peaks at 1294 cm^{-1}, corresponding to C–N stretching of secondary amines in the polymer, and at 1109 cm^{-1}, indicative of delocalized charges in the polymer backbone resulting from the formation of $–NH^+$ between benzenoid and quinoid rings [40], were also discerned. Vibrations in the range of 3000–3500 cm^{-1} were attributed to N–H stretching, and further differentiation of N–H secondary amine types was evident at 2978 cm^{-1} and 2843 cm^{-1}. CTAB, a surfactant, displayed distinctive peaks at 2850 cm^{-1} and 2918 cm^{-1}, arising from C–H stretching vibrations in methyl and methylene groups, overlapping with N–H stretching vibrations in PANI.

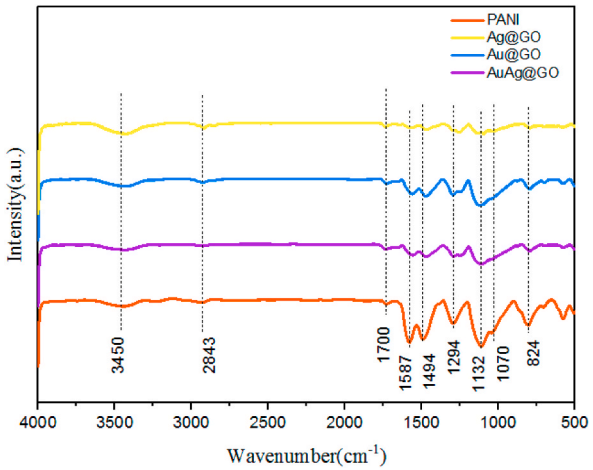

Fig. 1. FTIR spectra of PANI, Au_{20}@GO/PANI, Ag_{10}@GO/PANI and $Au_{15}Ag_{15}$@GO/PANI nanocomposites.

GO, known for its oxygen-functionalized groups, exhibited notable peaks at around 3450, 1700, and 1100 cm^{-1}, corresponding to O–H, C═O, and C–O groups, respectively. Hydroxyl peaks were evident at 3400 cm^{-1}, with an additional peak at 1070 cm^{-1} attributed to epoxy groups. In core/shell nanocomposites, a minor peak at approximately 1700 cm^{-1} was observed, associated with carbonyl groups. The comparatively low intensity of this carbonyl peak, in comparison to the PANI characterization peaks, can be attributed to the low concentration of GO sheets in the nanocomposite.

Notably, the FTIR analysis of Au_{20}@GO/PANI, Ag_{10}@GO/PANI, and $Au_{15}Ag_{15}$@GO/PANI nanocomposites unveiled shifts in the PANI peaks towards lower wavenumbers, along with a reduction in peak intensity. These FTIR shifts were notably amplified with the introduction of Au and Ag nanoparticles, signifying significant alterations in the PANI structure resulting from interactions between the nanoparticles and the nitrogen units in the PANI backbone.

3.2. X-ray diffraction (XRD) analysis

X-ray diffraction (XRD) patterns of PANI, Au_{20}@GO/PANI, Ag_{10}@GO/PANI, and $Au_{15}Ag_{15}$@GO/PANI nanocomposites are illustrated in Fig. 2. The diffraction peaks observed at 15°, 20°, and 25° can be confidently assigned to the (011), (020), and (200) crystal planes of PANI [31], respectively, providing critical structural information about the polymer.

In the Au_{20}@GO/PANI sample, distinct peaks characteristic of gold nanoparticles (Au NPs) are visible at 2Θ angles of 38° (111), 44° (200), 64° (220), and 78° (311) (corresponding to JCPDS card No. 01–1172). Likewise, in the case of the Ag_{10}@GO/PANI sample, silver nanoparticles (Ag NPs) exhibit their own distinctive peaks at 2Θ values of 33° (111), 42° (200), 65° (220), and 77° (311) (in accordance with JCPDS card NO. 04–0783) [41]. These specific peaks affirm the presence and crystalline nature of both Au and Ag nanoparticles within the nanocomposites. Notably, the formation of these characteristic peaks in the XRD patterns signifies the successful integration of Au and Ag nanoparticles during in-situ PANI synthesis.

Furthermore, an additional peak at approximately $2\Theta = 10°$ is evident, indicating an interlayer distance of 0.88 nm within the graphene oxide (GO) sheets, as calculated using Bragg's equation. This finding underscores the structural arrangement of GO within the nanocomposites and its role in the overall composite structure.

It is worth noting that cetyltrimethylammonium bromide (CTAB), a surfactant, displays characteristic peaks at 17°, 20°, and 23°, which, notably, overlap with some of the peaks associated with PANI [42]. The coexistence of these peaks is highlighted in Fig. 2, underscoring the presence and influence of CTAB within the nanocomposite structure, which can have implications for the composite's properties and performance.

The crystallinity and structure of four nanocomposite samples, namely Au_{20}@GO/PANI, Ag_{10}@GO/PANI, PANI, and $Au_{15}Ag_{15}$@GO/PANI, were investigated through XRD (X-ray diffraction) analysis. In this study, the Full Width at Half Maximum (FWHM) values obtained from the XRD tests were crucial indicators of the nanocomposites' structural characteristics. For Au_{20}@GO/PANI, the FWHM value of 5.1 suggests a moderate crystallinity, indicating a well-defined crystal structure with some degree of disorder. The presence of gold nanoparticles (Au NPs) on graphene oxide (GO) and polyaniline (PANI) may contribute to the observed crystalline features. Similarly, Ag_{10}@GO/PANI exhibits a FWHM value of 5.3, indicating a comparable crystallinity to Au_{20}@GO/PANI. The incorporation of silver nanoparticles (Ag NPs) into the nanocomposite, along with GO and PANI, contributes to the overall crystalline structure. PANI, with a tubular structure when used without nanoparticles, exhibits a FWHM value of 5.5. The slightly higher FWHM suggests a moderate crystallinity. On the other hand, $Au_{15}Ag_{15}$@GO/PANI exhibits a FWHM value of 4.3, indicating a slightly narrower peak compared to PANI. This suggests a higher crystallinity for $Au_{15}Ag_{15}$@GO/PANI, possibly influenced by the combination of gold and silver nanoparticles along with GO and PANI. In summary, the XRD results suggest that the nanocomposites Au_{20}@GO/PANI and Ag_{10}@GO/PANI have similar crystallinities, while PANI exhibits moderate crystallinity. The $Au_{15}Ag_{15}$@GO/PANI nanocomposite shows a slightly higher crystallinity compared to PANI, possibly due to the combination of different metal

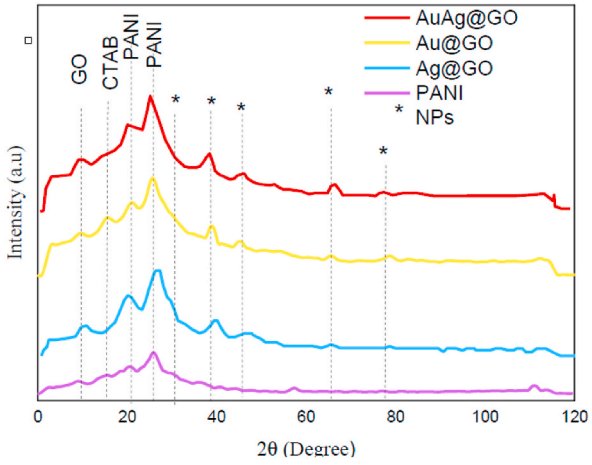

Fig. 2. XRD patterns of PANI, Au_{20}@GO/PANI, Ag_{10}@GO/PANI and $Au_{15}Ag_{15}$@GO/PANI nanocomposites.

nanoparticles. These findings provide valuable insights into the structural characteristics of the nanocomposites, paving the way for a deeper understanding of their properties and potential applications.

3.3. Elemental and structural analysis of prepared nanocomposites

The utilization of Field Emission Scanning Electron Microscopy (FESEM) images has been instrumental in highlighting the significant impact of various volumes of cetyltrimethylammonium bromide (CTAB) (at a concentration of 15 mM) on the structural configuration of polyaniline (PANI), as depicted in Fig. 3. The introduction of CTAB, which acts as a soft template, has brought about notable structural transformations in PANI, which can be favorably compared to the unaltered PANI structure presented in Fig. 3. In the absence of CTAB, PANI exhibits an amorphous morphology devoid of any tubular structure. However, with the incorporation of CTAB, PANI undergoes a remarkable transformation, adopting a more organized and structured configuration. Notably, at lower CTAB volumes, the dominance of the tubular structure is less pronounced, a consequence of the diminished CTAB concentration. Optimal results, in terms of achieving a well-defined tubular PANI structure, are observed when CTAB is added in the range of 10–20 mL (at 15

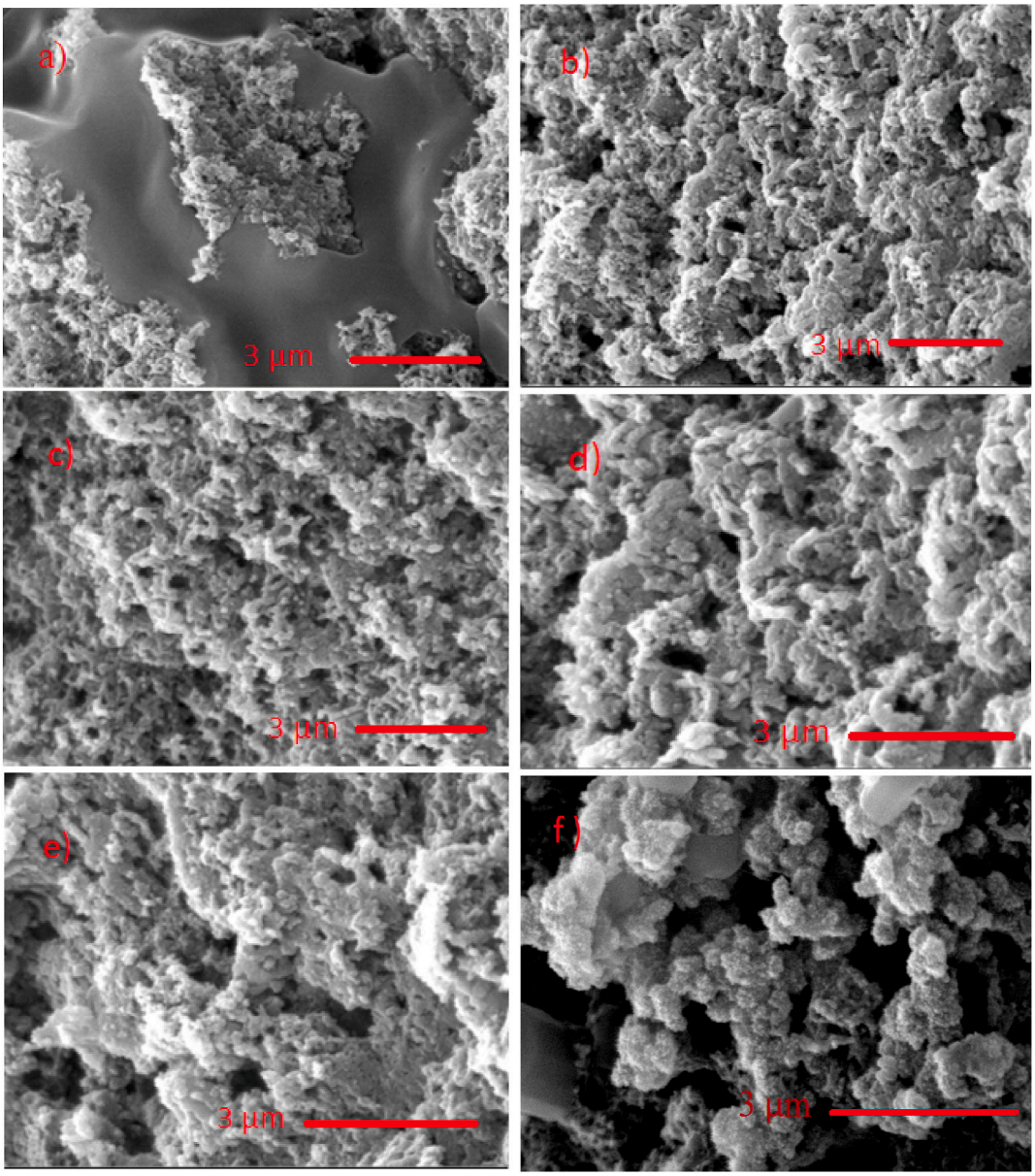

Fig. 3. SEM images of PANI with adding different volumes a) 5 mL, b) 10 mL, c) 15 mL, d) 20 mL, e) 25 mL of CTAB and f) no CTAB, during PANI polymerization.

mM concentration), as described in Fig. 3.

The structural configurations of the synthesized nanocomposites are illustrated in Fig. 3a-c, while Fig. 3f represents the PANI structure with no CTAB. Fig. 3 illustrates SEM images of PANI with adding different volumes of 5 mL (a), 10 mL (b), 15 mL (c), 20 mL (d), 25 mL (e) of CTAB and f) no CTAB, during PANI polymerization. The underlying principle governing the effect of CTAB on PANI transformation is elucidated in Scheme 2. CTAB, a surfactant, is characterized by a positively charged polar head and a nonpolar tail. In an aqueous environment, CTAB molecules form micellar structures. During the synthesis of PANI, these CTAB micelles aggregate into a rod-like arrangement, while aniline monomers are attracted to the amine groups of CTAB, initiating the polymerization process. As the polymerization proceeds, the PANI encapsulates the rod-shaped CTAB micelles. Subsequent washing steps with water, acetone, and HCl solution lead to the removal of CTAB molecules, leaving behind a tubular PANI structure. This tubular PANI exhibits enhanced conductivity and superior dispersibility in water, distinguishing it from the amorphous PANI.

With the optimal concentration of CTAB for tubular PANI synthesis established, solutions containing Au_{20}@GO, Ag_{20}@GO, and $Au_{15}Ag_{15}$@GO core/shell nanoparticles (NPs) were introduced with 10 mL of CTAB to investigate their influence on the PANI structure. The addition of these prepared nanocomposites has had a pronounced positive effect on the development of tubular PANI structures. In the Au_{20}@GO/PANI sample, certain amorphous regions were initially evident, but these disappeared upon the introduction of Ag NPs (as depicted in Fig. 4). Fig. 4 illustrates FESEM images of Au@GO/PANI (a), Ag@GO/PANI (b), AuAg@GO/PANI nanocomposites (c), close look of Au@GO/PANI (a'), Ag@GO/PANI (b'), AuAg@GO/PANI nanostructure (c'), EDX patterns of Au@GO/PANI (a''), Ag@GO/PANI (b''), and AuAg@GO/PANI (c''). This intriguing phenomenon can be attributed to the strong interaction between the PANI backbone and the π-π bonds in graphene oxide [43,44]. When core/shell nanoparticles are introduced to aniline during the synthesis process, they engage with the polymer backbone, as elucidated in Scheme 3. Particles that are not absorbed by the PANI backbone are effectively eliminated through repeated washing steps. Elemental mapping has corroborated the presence of gold and silver nanoparticles, revealing a uniform dispersion of these NPs within the samples.

Additionally, we investigated the presence of oxygen atoms to assess the dispersion of graphene oxide (GO), revealing that oxygen atoms were uniformly distributed near gold and silver nanoparticles. This distribution is depicted in Fig. 5, which illustrates elemental map images of: a) silver (Ag), b) gold (Au), c) oxygen (O) atoms, d) carbon (C), e) silver and gold atoms (Ag and Au), and f) silver, gold, oxygen, and carbon atoms (Ag, Au, O, and C) in the $Au_{15}Ag_{15}$@GO/PANI nanocomposite. Energy-Dispersive X-ray (EDX) analysis further confirmed the presence of gold, silver, and oxygen atoms, substantiating the integration of Au@GO and Ag@GO structures within the PANI nanocomposites.

3.4. Thermogravimetric analysis

Thermogravimetric analysis (TGA) was conducted on both pristine PANI and $Au_{15}Ag_{15}$@GO/PANI samples, as depicted in Fig. 6a. Existing literature has established that PANI experiences three notable weight loss stages, each occurring at distinct temperature ranges: approximately 100 °C, 300 °C, and 500 °C. These stages correspond to the removal of moisture, the exclusion of doping ions from the polymer structure, and the eventual degradation of the polymer backbone, respectively [45,46].

In the initial temperature range, between 30 °C and 100 °C, the analysis aimed to eliminate any moisture present in both the PANI and nanocomposite samples. The results indicated that $Au_{15}Ag_{15}$@GO/PANI retained a higher quantity of water molecules. This propensity is attributed to the hydrophilic nature imposed upon the nanocomposite by the presence of Au@GO, Ag@GO, and CTAB components.

Within the temperature range of 400 °C–500 °C, a notable mass loss occurred, signifying the stage of doping in the $Au_{15}Ag_{15}$@GO/PANI sample. This weight loss is indicative of the expulsion of doping ions as the sample undergoes thermal decomposition.

Subsequently, as the temperature was raised further, approximately between 500 °C and 550 °C, the polymer backbone underwent decomposition, leading to a more pronounced weight loss in the $Au_{15}Ag_{15}$@GO/PANI nanocomposite. This phenomenon suggests that the bulk structure of PANI exhibited a higher degree of thermal stability in comparison to the nanotube structure of $Au_{15}Ag_{15}$@GO/

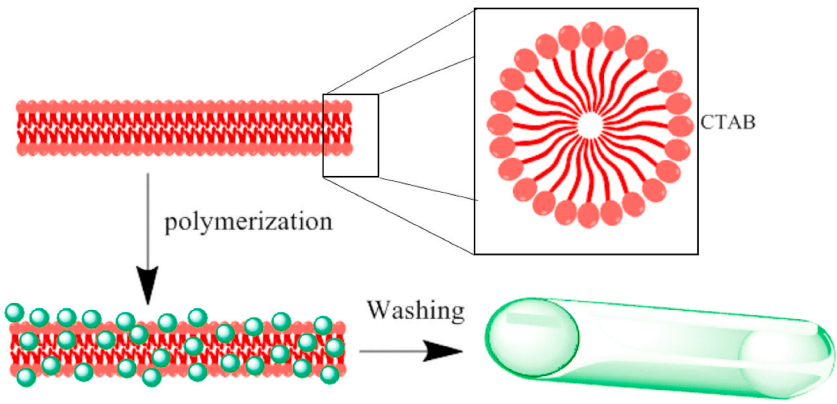

Scheme 2. Tubular polyaniline synthesis using CTAB as a soft template.

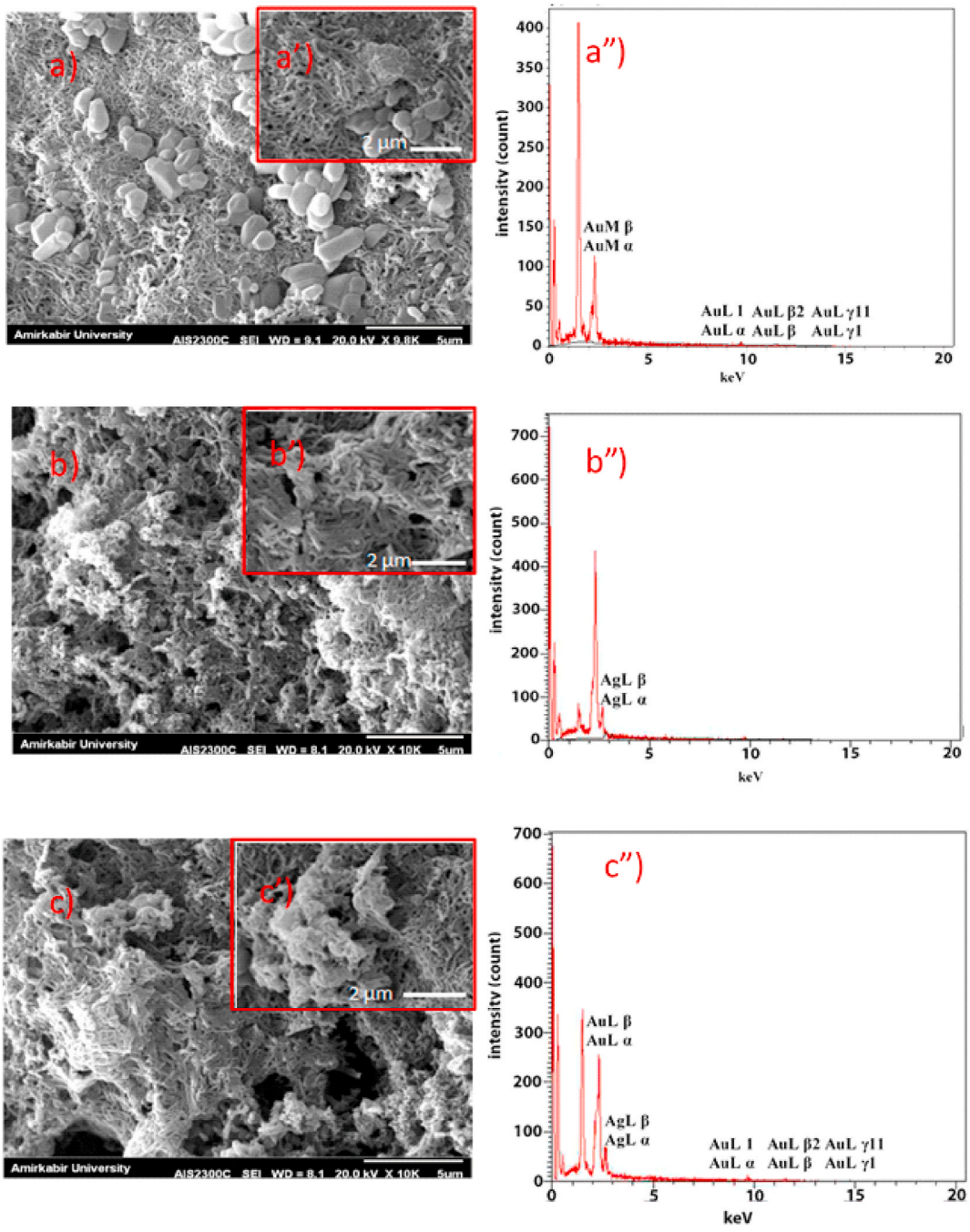

Fig. 4. FESEM images of a) Au_{20}@GO/PANI b) Ag_{10}@GO/PANI, c) $Au_{15}Ag_{15}$@GO/PANI nanocomposites, close look of a') Au_{20}@GO/PANI, b') Ag_{10}@GO/PANI, c') $Au_{15}Ag_{15}$@GO/PANI nanostructure, EDX patterns of a'') Au_{20}@GO/PANI, b'') Ag_{10}@GO/PANI and c'') $Au_{15}Ag_{15}$@GO/PANI.

PANI. A Transmission Electron Microscopy (TEM) image in Fig. 6b depicts the nanotube structure of $Au_{15}Ag_{15}$@GO/PANI. This structural analysis provides essential insights into the intricate nanocomposite architectures and their potential applications. The nanotube structure, with its enhanced heat transfer properties, exhibited a more accelerated decomposition under the higher temperature conditions. This insight provides valuable information regarding the thermal behavior and stability of these materials, critical for various potential applications.

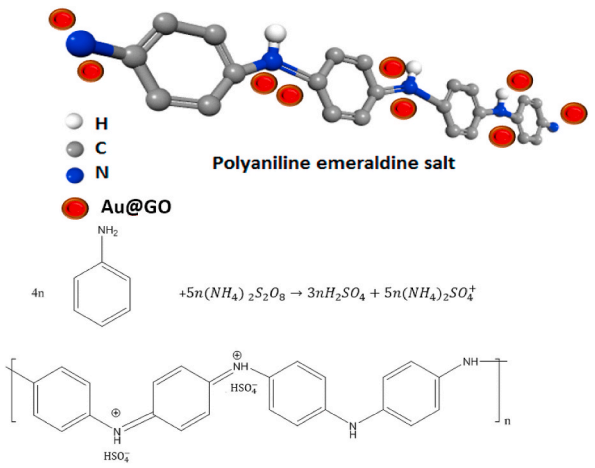

Scheme 3. Schematic polymerization mechanism of emeraldine salt of polyaniline in the presence of Au@GO nanoparticles using APS.

3.5. Impact of solvents on PANI solubility and conductivity

The UV–Visible (UV–Vis) spectra of PANI nanotubes incorporated with Au_{20}@GO/PANI, Ag_{10}@GO/PANI, and $Au_{15}Ag_{15}$@GO/PANI, in three distinct solvents—NMP, water, and DMSO—are presented in Fig. 7a–c, respectively. PANI exhibits two prominent absorption peaks at 315 nm and 455 nm. The absorption at 315 nm corresponds to the π-π* transition within benzenoid rings, while the peak at 455 nm arises from polaron-π* transitions. Additionally, a broader peak within the 700–800 nm range corresponds to π-polaron transitions [8,47,48]. These polaronic transition peaks serve as an indicator of the presence of charge carriers in PANI. The ratio of the polaronic band (750 nm) to the π-π* (315 nm) transition band, denoted as I_{750}/I_{315}, provides insights into the average oxidation state of PANI. The results, compiled in Table 2 for ease of comparison, reveal that the doping state of the three samples is influenced by the choice of solvents. In NMP, a significant reduction in the I_{750}/I_{315} ratio suggests dedoping of PANI, attributed to the formation of hydrogen bonds (C═O···N–H) between the C═O groups present in NMP and the amine groups of PANI [49]. The trend observed for doping preservation in the various solvents is as follows: water > DMSO > NMP. This order suggests that water has the least adverse effect on the doping status of PANI.

Both gold nanoparticles (Au NPs) and graphene oxide (GO) exhibit unique absorption characteristics. Au NPs display plasmonic absorption at approximately 520 nm, while GO has characteristic peaks at around 250 nm and 300 nm, corresponding to the π-π and π-π* transitions within hexagonal carbonic and oxygen-containing groups, respectively. The relatively strong absorbance of benzenoid and imine groups in PANI, in comparison to the absorption of Au NPs and GO, makes the plasmon absorption less visible.

The solubility of PANI nanocomposites in water, NMP, and DMSO is visually represented in Fig. 7a'-c'. Specifically, 4 mg/mL of Au_{20}@GO/PANI, Ag_{10}@GO/PANI, and $Au_{15}Ag_{15}$@GO/PANI were dispersed in each of the solvents, followed by stirring for 3 h at room temperature. In NMP and DMSO, the PANI dispersion remained stable for several weeks, indicating good solubility. However, in water, the dispersion settled after 3 h. Initially, all mixtures exhibited a green color, but after 2 days, the mixture of $Au_{15}Ag_{15}$@GO/PANI in NMP transitioned to a blue color. This color change is indicative of the dedoping of emeraldine salt to emeraldine base, a phenomenon consistent with the UV–Vis results. Conversely, the color of the nanocomposite remained green in DMSO even after 1 week, highlighting its sustained doping state. These solubility and dedoping characteristics hold significant implications for the practical use and processing of these materials.

The emeraldine salt form of PANI is characterized by the presence of one molecule of hydrochloric acid per every two aniline units. This specific composition imparts ionic conductivity to PANI. The acidic hydrogen within the emeraldine salt interacts with the imino groups of PANI, which exhibit a high degree of conjugation. Furthermore, this interaction between polarons and anions, a component of the acid, serves to neutralize positive charges [50,51]. This combination of factors contributes to PANI's ionic conductivity.

The ionic conductivity of the prepared Au_{20}@GO/PANI, Ag_{10}@GO/PANI, and $Au_{15}Ag_{15}$@GO/PANI samples was assessed in various solvents, and the results demonstrated that the PANI nanocomposites exhibited the highest ionic conductivity in the following order: water > DMSO > NMP. The comprehensive dataset is summarized in Table 3. The comparatively lower ionic conductivity observed in NMP can be attributed to the higher degree of dedoping experienced by PANI, a finding that aligns with the UV–Vis results. This conductivity data provides essential insights into the electrochemical properties and performance of these nanocomposites in different solvent environments, which is vital information for various potential applications.

3.6. Gas sensor analysis

To evaluate gas sensing performance, the most promising metal nanocomposites, selected based on their superior conductivity and nanotube structure, were meticulously deposited (using a 50 μL drop-casting method) onto comb-like gold electrodes, as depicted in Scheme 4. The selected nanocomposites, namely Au_{20}@GO/PANI, Ag_{10}@GO/PANI, and $Au_{15}Ag_{15}$@GO/PANI, were dissolved in water

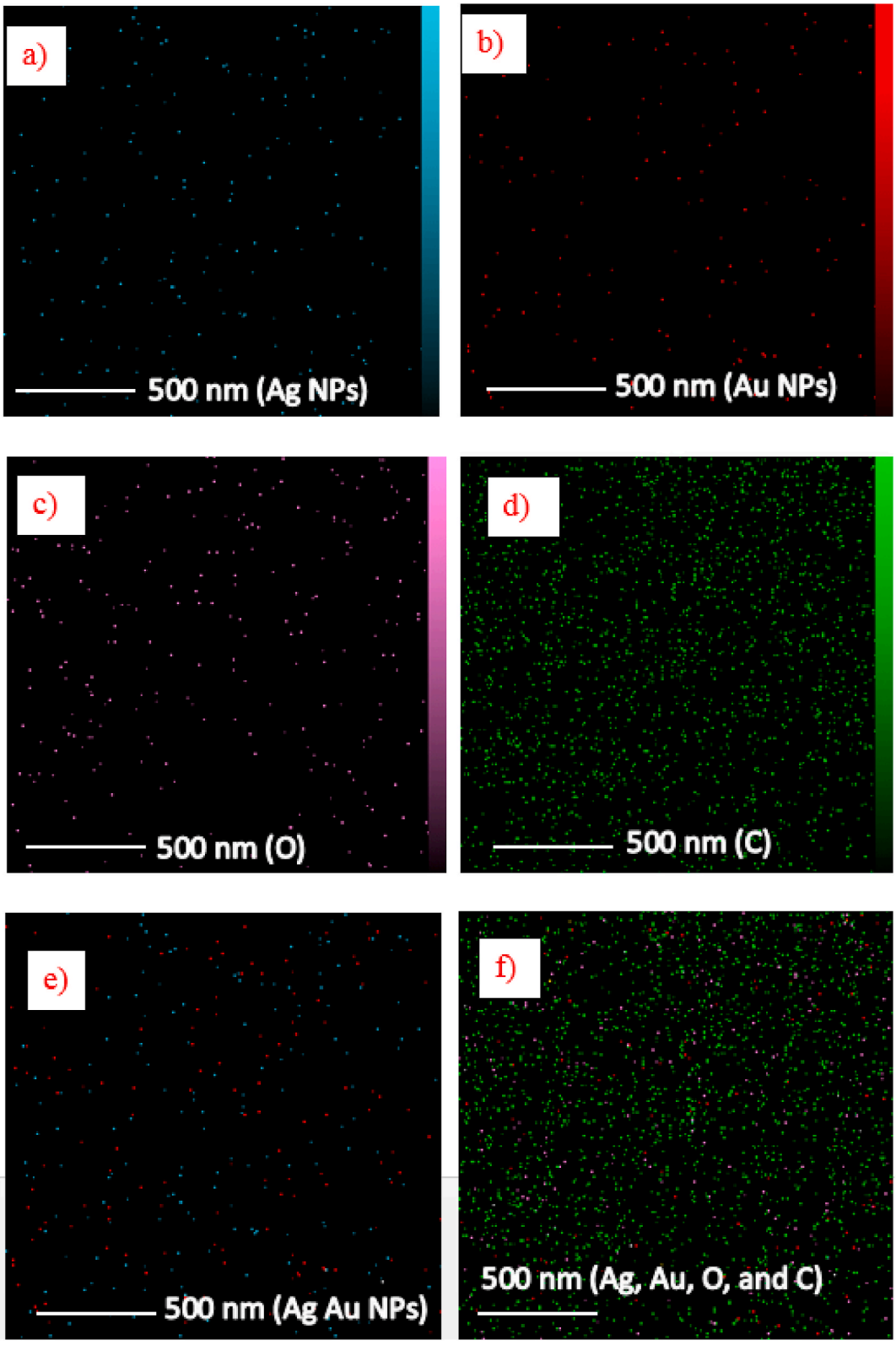

Fig. 5. Illustrates elemental map images of a) Ag, b) Au, c) oxygen (O) atoms, d) carbon (C), e) Ag and Au atoms, and f) Ag, Au, O, and C atoms in $Au_{15}Ag_{15}$@GO/PANI nanocomposite.

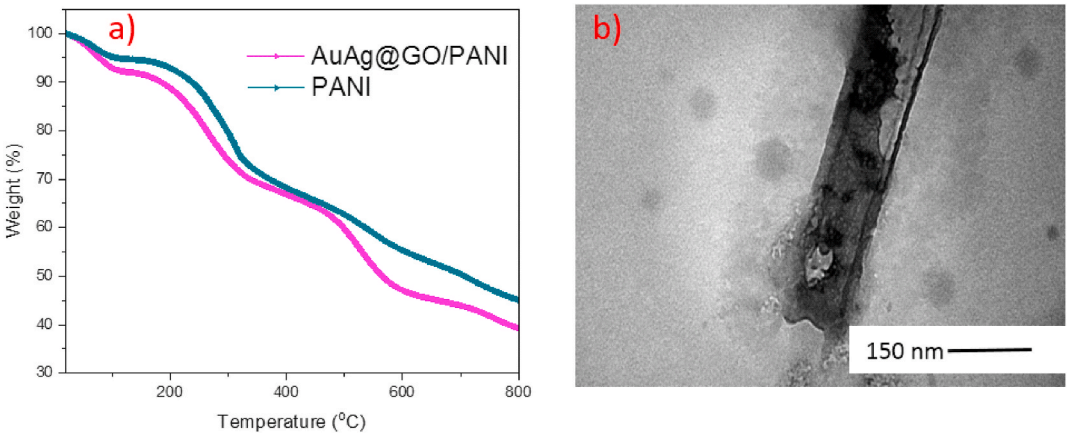

Fig. 6. a) TGA curves of PANI and $Au_{15}Ag_{15}$@GO/PANI nanocomposite, b) TEM image of tubular $Au_{15}Ag_{15}$@GO/PANI nanostructure.

and then meticulously applied to the gold electrodes.

Subsequently, three different gases—nitrogen dioxide (NO_2), carbon dioxide (CO_2), and hydrogen sulfide (H_2S)—were employed to assess the gas sensing efficiency and retention time of the meticulously prepared nanocomposites. The responsiveness of these sensor systems was quantitatively defined through the utilization of Equation (1):

$$\Delta R/R_0\,\% = \frac{R_g - R_0}{R_0} * 100 \tag{1}$$

here, R_g represents the resistance of the sensor when exposed to the target gas, and R_0 is the resistance of the sensor when exposed to air.

The nanotube structure of the PANI film, owing to its significantly larger surface area when compared to shapeless PANI, enhances its interactions with gases [52]. Moreover, the metal nanoparticles play a catalytic role, as evidenced by the observed reduction in sensor resistance upon exposure to NO_2. It is essential to note that the conductivity of PANI is not solely determined by the degree of protonation but is also influenced by the degree of oxidation. Reports in the literature have documented a decline in the resistance of PANI upon contact with NO_2, in line with our understanding of the oxidative nature of NO_2 gas. When an oxidizing agent, such as NO_2, comes into contact with the π-electrons of PANI, electrons are transferred from PANI to NO_2. As a result, the positively charged P-type PANI experiences an increased density of holes relative to electrons. This augmented charge carrier density contributes to higher conductivity in PANI. The presence of metal nanoparticles, with their catalytic properties, can further facilitate charge transfer and enhance response efficiency. The transient resistance profiles of gas sensors utilizing Au_{20}@GO/PANI, Ag_{10}@GO/PANI, and $Au_{15}Ag_{15}$@GO/PANI in contact with NO_2 are depicted in Fig. 8a. The response and recovery times of PANI and $Au_{15}Ag_{15}$@GO/PANI sensors towards NO_2 are illustrated in Fig. 9a and a', respectively. Notably, the response time for PANI is 883 s, whereas $Au_{15}Ag_{15}$@GO/PANI exhibits a significantly reduced response time of 431 s. The recovery time for PANI is 445 s, while $Au_{15}Ag_{15}$@GO/PANI showcases an even swifter recovery time of 296 s.

Furthermore, H_2S was effectively detected by the sensors composed of Au_{20}@GO/PANI, Ag_{10}@GO/PANI, and $Au_{15}Ag_{15}$@GO/PANI nanocomposites, as illustrated in Fig. 8b. Prior research has indicated that H_2S interacts with gold nanoparticles, forming AuS, which results in the generation of H+ ions (as shown in Equation (2)) and, consequently, a reduction in the resistance of Au_{20}@GO/PANI and $Au_{15}Ag_{15}$@GO/PANI nanocomposites [53,54]. Silver nanoparticles also interact with H_2S (as described in Equation (3)), although to a lesser extent than the interaction between Au and H_2S. The chemical equations involved are presented below:

These reactions elucidate the mechanistic foundations of H_2S detection and provide insights into the sensor's sensitivity and selectivity.

$$H_2S + Au \rightarrow AuS + 2H^+ \tag{2}$$

$$H_2S + Ag \rightarrow AgS + 2H^+ \tag{3}$$

The response and recovery times of PANI and $Au_{15}Ag_{15}$@GO/PANI sensors towards H_2S are illustrated in Fig. 9b and b', respectively. Notably, the response time for PANI is 929 s, whereas $Au_{15}Ag_{15}$@GO/PANI exhibits a significantly reduced response time of 335 s. The recovery time for PANI is 807 s, while $Au_{15}Ag_{15}$@GO/PANI showcases an even swifter recovery time of 277 s. These results unequivocally demonstrate that the inclusion of Au and Ag nanoparticles enhances the sensing capabilities of the nanocomposite when compared to pristine PANI.

Furthermore, the sensors based on Au_{20}@GO/PANI, Ag_{10}@GO/PANI, and $Au_{15}Ag_{15}$@GO/PANI were evaluated for their response to carbon dioxide (CO_2), revealing superior sensing performance compared to PANI-based sensors. The underlying sensing mechanism for PANI and PANI nanocomposites in the context of CO_2 detection hinges on two key mechanisms. First, primary amines are capable of interacting with CO_2 to form carbamates. To effectively trap CO_2, the involvement of two primary amines is required, as illustrated in

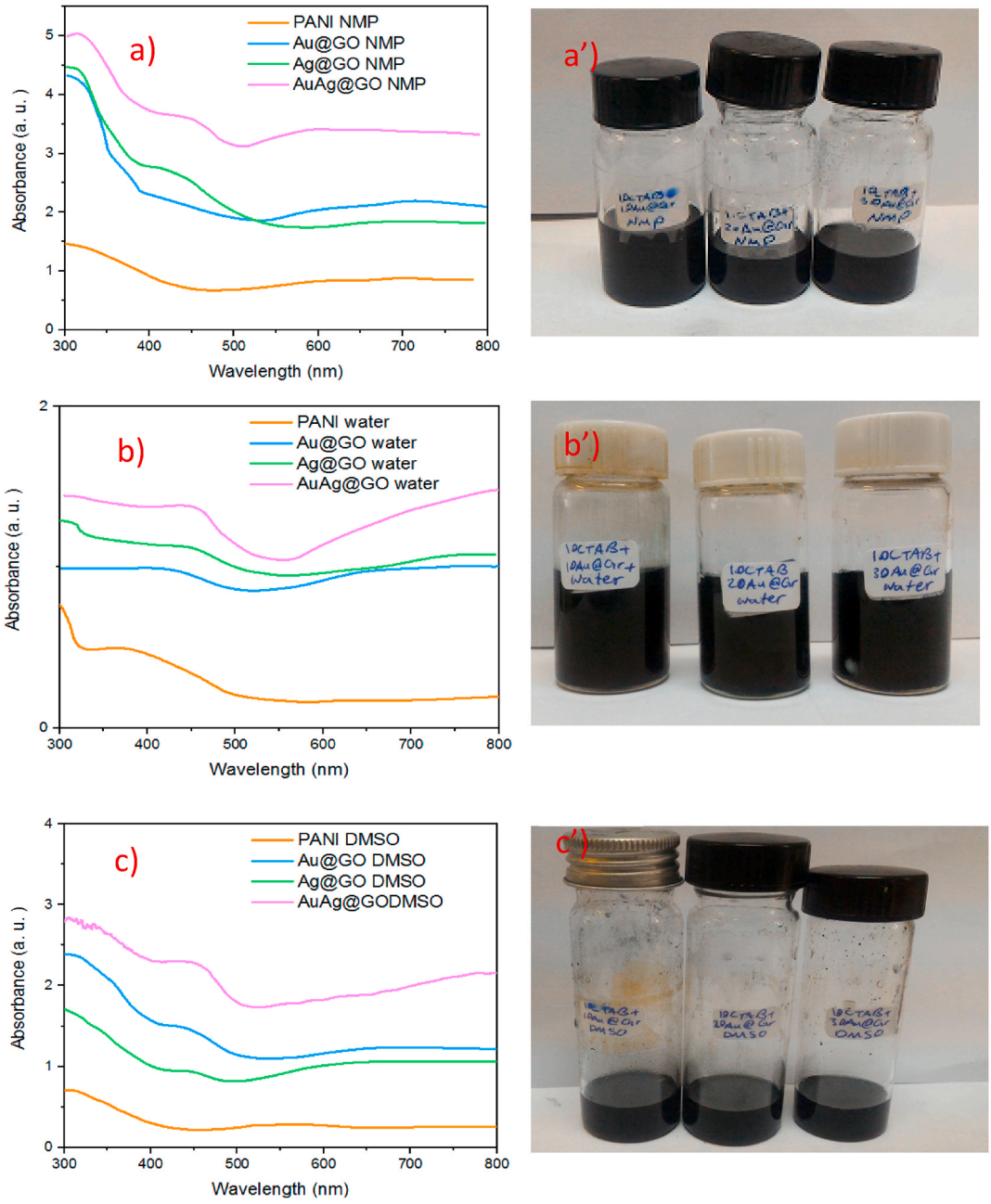

Fig. 7. UV–Vis absorbance and solubility of PANI, Au_{20}@GO/PANI, Ag_{10}@GO/PANI and $Au_{15}Ag_{15}$@GO/PANI samples in a, a') NMP, b, b') water and c, c') DMSO solvents respectively.

Table 2
Intensity ratio of I_{750}/I_{315} of Au_{20}@GO/PANI, Ag_{10}@GO/PANI, $Au_{15}Ag_{15}$@GO/PANI samples.

	I_{750}/I_{315}		
Sample name	Water	DMSO	NMP
Au_{20}@GO/PANI	1.01	0.52	0.51
Ag_{10}@GO/PANI	0.84	0.47	0.40
$Au_{15}Ag_{15}$@GO/PANI	1.00	0.75	0.66
PANI	0.31	0.37	0.59

Table 3
Ionic conductivity of Au_{20}@GO/PANI, Ag_{10}@GO/PANI, and $Au_{15}Ag_{15}$@GO/PANI samples in water, DMSO, NMP solvents.

	Conductivity in solvents (μs)		
Sample name	**Water**	**DMSO**	**NMP**
Au_{20}@GO/PANI	1667	108	42
$Au_{15}Ag_{15}$@GO/PANI	1982	91	49
Ag_{10}@GO/PANI	997	140	13

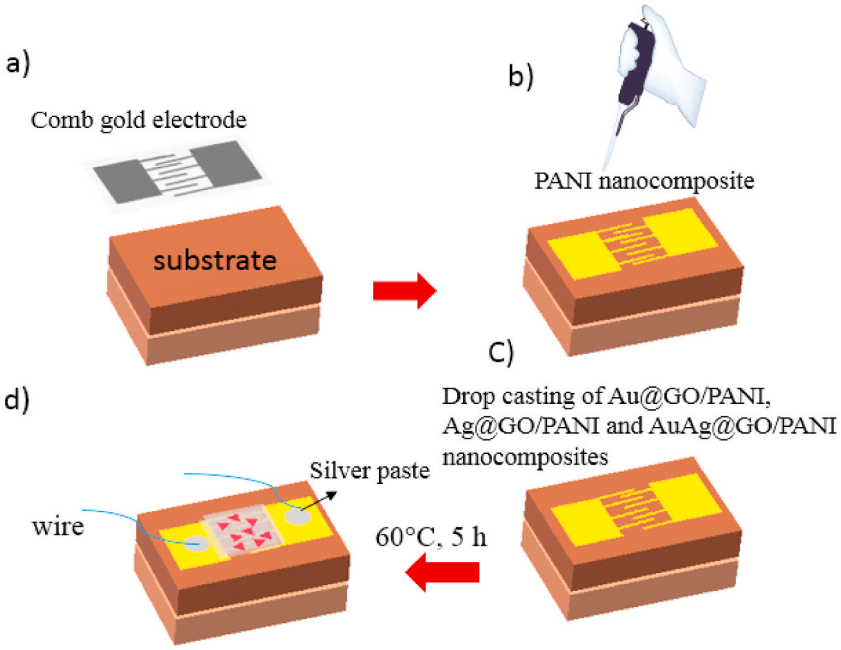

Scheme 4. Schematic preparation of gas sensor based on prepared metal nanocomposites.

Equation (4):

$$CO_2 + 2RNH_2 \leftrightarrow RNHCOO^- + RNH_3^+ \quad (4)$$

This mechanistic insight underscores the sensitivity of the nanocomposite sensors to CO_2, elucidating the improved sensing efficiency of Au_{20}@GO/PANI, Ag_{10}@GO/PANI, and $Au_{15}Ag_{15}$@GO/PANI in comparison to their PANI-based counterparts.

In this intricate process, a pair of amine electrons forms a bond with the carbon atom of CO2, leading to the creation of a zwitterion. Subsequently, another amine group dissociates a proton from the zwitterion, resulting in the formation of carbamate [55,56]. This dual interaction signifies a reduction in the number of free amine groups and, in turn, a decrease in the charge density of protons. Consequently, the net effect is an increase in electrical resistance.

Alternatively, the second scenario unfolds with the formation of a p-n junction between the Au and Ag nanoparticles (NPs) and PANI. In this instance, a depletion layer is established at the interface of the metal NPs and PANI. When CO_2 is introduced into the chamber, PANI nanocomposites adsorb CO_2 molecules, liberating electrons within the junction. This phenomenon augments the thickness of the depletion layer, subsequently elevating the electrical resistance [54]. Fig. 8c represents the transient resistance profiles of gas sensors employing nanocomposites in response to CO_2. The response and recovery times for $Au_{15}Ag_{15}$@GO/PANI and PANI toward CO_2 are represented in Fig. 9c and c', respectively, and notably, $Au_{15}Ag_{15}$@GO/PANI achieves a swifter response time of 279 s and a more rapid recovery time of 366 s, compared to the corresponding times of 592 s and 789 s for PANI alone. These findings explicitly underscore the enhanced response characteristics of the nanocomposite in contrast to PANI-based sensors, with both mechanisms contributing to their improved sensing efficiency. Acetone was also monitored and Au_{20}@GO/PANI, Ag_{10}@GO/PANI and $Au_{15}Ag_{15}$@GO/PANI based sensors showed better sensing in comparison with PANI-based sensor as shown in Fig. 8d. The transient resistance variation of the Sensors based on Au_{20}@GO/PANI, Ag_{10}@GO/PANI, and $Au_{15}Ag_{15}$@GO/PANI to different concentrations of acetone vapor are shown in Fig. 7d. Previous results investigated that some analytic gases, such as ketones, may change the crystallinity of conducting polymers [57]. The strong interaction between small ketones like acetone and nitrogen atoms of polyaniline led to the expansion of polyaniline chains to more stretching conformation [58]. As a result, polymer crystallinity increases, and electrical resistance declines. Fig. 9d and d' compare response and recovery times of PANI and $Au_{15}Ag_{15}$@GO/PANI sensors toward acetone which are 867 s, 672 s, and 193 s, 509 s, respectively.

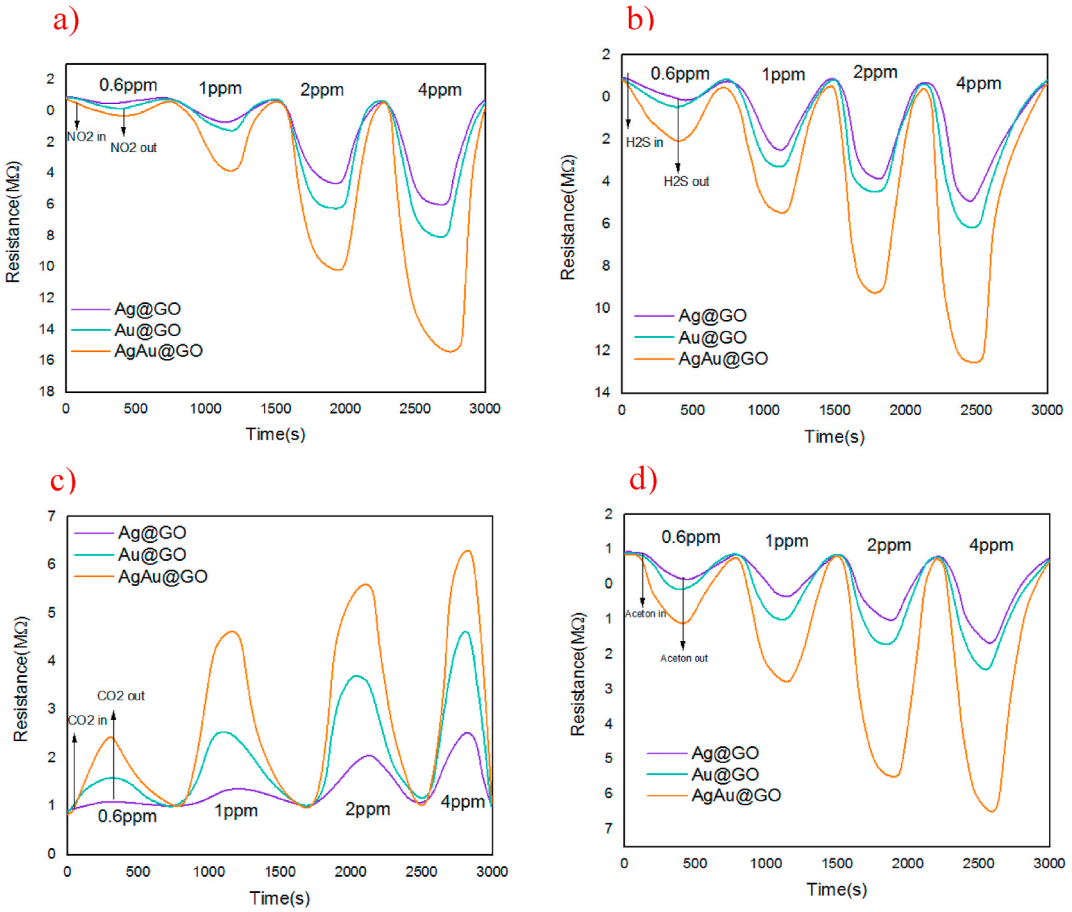

Fig. 8. Resistance of Au_{20}@GO/PANI, Ag_{10}@GO/PANI and $Au_{15}Ag_{15}$@GO/PANI nanocomposites gas sensors in contact with a) NO_2, b) H_2S, c) CO_2 gases, and d) acetone.

For enhanced comparability, all the sensor responses for the prepared sensors have been combined in Fig. 10. Fig. 10 illustrates selectivity of the PANI, Au_{20}@GO/PANI, Ag_{10}@GO/PANI and $Au_{15}Ag_{15}$@GO/PANI nanocomposite gas sensors toward 4 ppm of NO_2, H_2S, acetone, and CO_2 gases. Standard deviation (SD) values of the set of sensors are calculated using the following equation (5):

$$SD = \sqrt{\frac{\sum (Xi - X)^2}{N}} \tag{5}$$

Where X_i is each individual baseline measurement, X is the mean of the baseline measurements, and N is the number of baseline measurements. According to the calculations, the Au_{20}@GO/PANI has SD value of 0.3, 0.1, 0.2, and 0.2 in contact with NO_2, CO_2, H_2S, and acetone, respectively. Ag_{10}@GO/PANI has SD value of 0.3, 0.05, 0.2, and 0.2 in contact with NO_2, CO_2, H_2S, and acetone, respectively. $Au_{15}Ag_{15}$@GO/PANI nanocomposite gas sensor has SD value of 0.3, 0.1, 0.2, and 0.1 in contact with NO_2, CO_2, H_2S, and acetone, respectively. PANI gas sensor has SD value of 0.3, 0.07, 0.05, and 0.1 in contact with NO_2, CO_2, H_2S, and acetone, respectively.

For further analysis, detection limit (DL) of the sensors were measured using the following equation (6):

$$DL = K \times SD \tag{6}$$

In the abovementioned equation (6) K is a constant (K = 3). To obtain DL of the sensors, 4 blank samples were tested using each sensor. SD values of the sensors using blank sample were determined. The blank sample is a sample without analyte. DL of the sensors were calculated using SD values of the sensors. DL of the Au_{20}@GO/PANI gas sensor, Ag_{10}@GO/PANI gas sensor, and $Au_{15}Ag_{15}$@GO/PANI nanocomposite gas sensor are 0.6, 0.45, and 0.3, respectively.

Table 4 illustrates a comparison table showing response and recovery times of nanocomposites toward CO_2, NO_2, and H_2S gases studied by other researchers. As shown in Table 4, the present sensor based on $Au_{15}Ag_{15}$@GO/PANI shows detection range of 0.6–4, 1–4, 0.6–4 (ppm) for detecting NO_2, CO_2, and H_2S, respectively. Response time and recovery times of the sensor based on $Au_{15}Ag_{15}$@GO/PANI are compatible with other researches in this field.

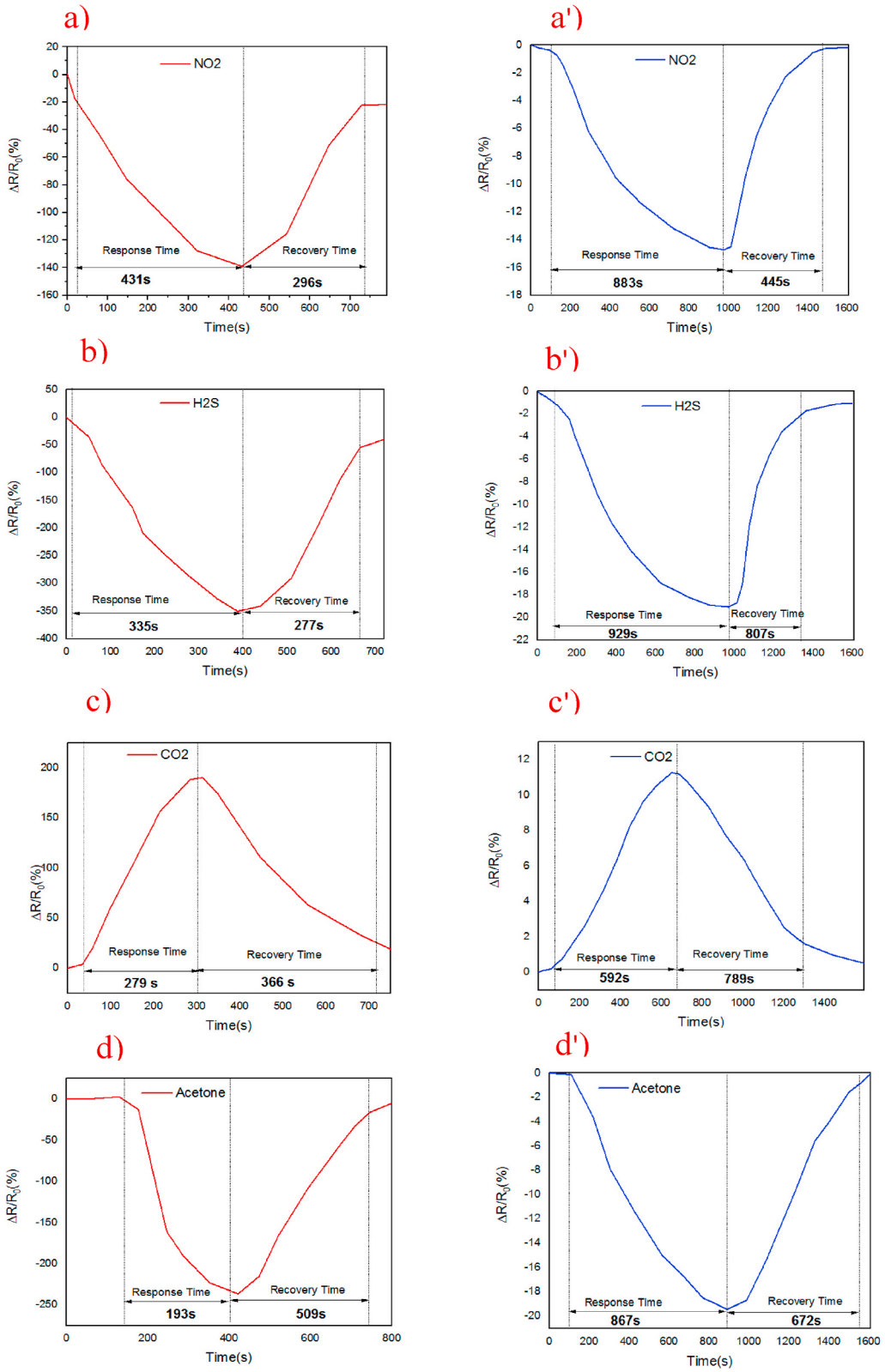

Fig. 9. Response and recovery times of the $Au_{15}Ag_{15}$@GO/PANI nanocomposite gas sensors to 1 ppm a) NO_2, b) H_2S, c) CO_2, and d) acetone and PANI gas sensor to 1 ppm a') NO_2, b') H_2S, c') CO_2, and d') acetone.

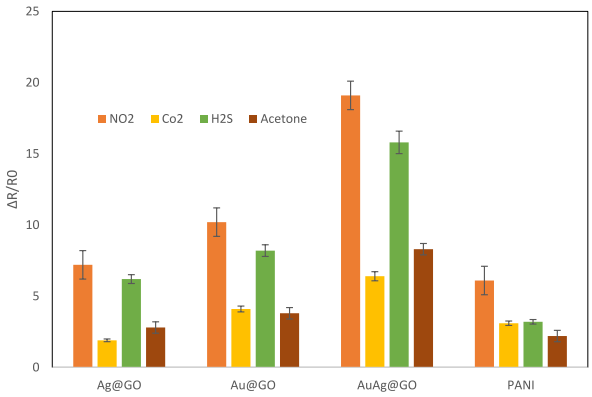

Fig. 10. Selectivity of the PANI, Au_{20}@GO/PANI, Ag_{10}@GO/PANI and $Au_{15}Ag_{15}$@GO/PANI nanocomposite gas sensors toward 4 ppm acetone, NO_2, H_2S, and CO_2 gases.

Fig. 11 presents the calibration curves depicting the responses of the set of sensors when in contact with various gases such as NO_2, CO_2, acetone, and H_2S. These curves serve as a visual representation of how the sensors' responses vary with different concentrations of each gas.

In addition to the curves, the accompanying equations of the linear trend lines are displayed on the graph. These trend lines help quantify the relationship between the sensor responses and the concentration of the gases. The equations are instrumental in determining the sensitivity of each sensor. Sensitivity is derived from the slope of the linear trend line in the calibration curve.

To calculate sensitivity, the following general formula can be employed:

Sensitivity = Change in Sensor Response/Change in Gas Concentration

The calculated sensitivity values for each sensor are then utilized to assess their performance in detecting different gases. The Au_{20}@GO/PANI gas sensor has sensitivity of 2.4085, 0.8303, 0.6221, and 1.1965 toward NO_2, CO_2, acetone, and H_2S, respectively. The Ag_{10}@GO/PANI gas sensor has sensitivity of 1.9194, 0.4117, 0.515, and 1.4341 toward NO_2, CO_2, acetone, and H_2S, respectively. The $Au_{15}Ag_{15}$@GO/PANI gas sensor has sensitivity of 4.2649, 0.9377, 1.4902, and 2.828 toward NO_2, CO_2, acetone, and H_2S, respectively. These sensitivity values offer insights into the sensors' ability to detect and respond to varying concentrations of specific gases. Higher sensitivity values generally indicate a more responsive sensor, making them crucial parameters for evaluating the efficacy of gas sensors in practical applications. As results show, $Au_{15}Ag_{15}$@GO/PANI gas sensor shows the highest sensitivity toward gases in comparison to the two other gas sensors. The results also indicates higher sensitivity of $Au_{15}Ag_{15}$@GO/PANI gas sensor toward NO_2.

4. Conclusion

We have successfully developed an efficient in-situ method for preparing Au@GO/PANI nanostructures, with CTAB acting as a soft template to precisely control the tubular structure of PANI. We conducted thorough analyses of the nanocomposite's dispersibility in various solvents, noting the highest ionic conductivity of 1982 μs in a nanocomposite/water dispersion, which significantly decreased to 49 μs in N-Methyl-2-pyrrolidone (NMP), confirming the dedoping effect of NMP. Importantly, the AuAg@GO/PANI nanocomposite exhibited exceptional sensing capabilities, surpassing PANI-based gas sensor devices in detecting CO_2, NO_2, and H_2S. Notably, at room temperature, the AuAg@GO/PANI nanocomposite displayed rapid response times of 279, 431, and 335 s, along with efficient recovery times of 366, 296, and 277 s when exposed to 1 ppm concentrations of CO_2, NO_2, and H_2S, respectively. In contrast, PANI exhibited significantly slower response and recovery times for the same gases, highlighting the enhancing role of core@shell nanoparticles in gas sensor performance. Additionally, the AuAg@GO/PANI nanocomposite offers an environmentally friendly and cost-effective solution-processing method for fabricating efficient gas sensors. This research underscores the potential of the proposed architecture in various applications, including sensors, optoelectronics, and energy conversion."

CRediT authorship contribution statement

Zahra babaei: Writing – original draft, Methodology, Conceptualization. **Bahareh Rezaei:** Writing – original draft, Data curation. **Ehsan Gholami:** Data curation. **Faramarz Afshar Taromi:** Writing – review & editing, Supervision. **Amir Hossein Haghighi:** Writing – review & editing, Supervision.

Declaration of competing interest

The authors declare that they have no known competing financial interests or personal relationships that could have appeared to

Table 4
Comparison table showing response and recovery times of nanocomposites toward CO_2, NO_2, acetone, and H_2S gases studied by other researchers.

Gas	Sample	Detection range (ppm)	Response time	Recovery time	Operating temperature	Reference
NO_2	**Au NP-MWCNTs**	**0.1–1**	**>600**	**-**	**RT.**	[59]
	Au NP-rGO	**0.5–5**	**132**	**386**	**50°C**	[60]
	$Au_{15}Ag_{15}$@GO/PANI	**0.6–4**	**431**	**296**	**RT.**	**present paper**
CO_2	**PANI/chloroalumium phthalocyanine**	**0.05–7.20**	**250**	**200**	**27°C**	[61]
	Amino-functionalized Gr/PANI nanofiber	**20–2000**	**10**	**20**	**RT.**	[62]
	$Au_{15}Ag_{15}$@GO/PANI	**1–4**	**279**	**366**	**RT.**	**present paper**
H_2S	**PANI/$CuCl_2$**	**2.5–100**	**1000**	**-**	**20°C**	[63]
	PANI/Au	**0.1–100 (ppb)**	**<120**	**<300**	**RT.**	[53]
	$Au_{15}Ag_{15}$@GO/PANI	**0.6–4**	**335**	**277**	**RT.**	**present paper**
Acetone	**ZnO/graphene quantum dots (GQDs)/PANI**	**500**	**15**	**27**	**25°C**	[57]
	$Au_{15}Ag_{15}$@GO/PANI	**0.6–4**	**193**	**509**	**RT.**	**This paper**

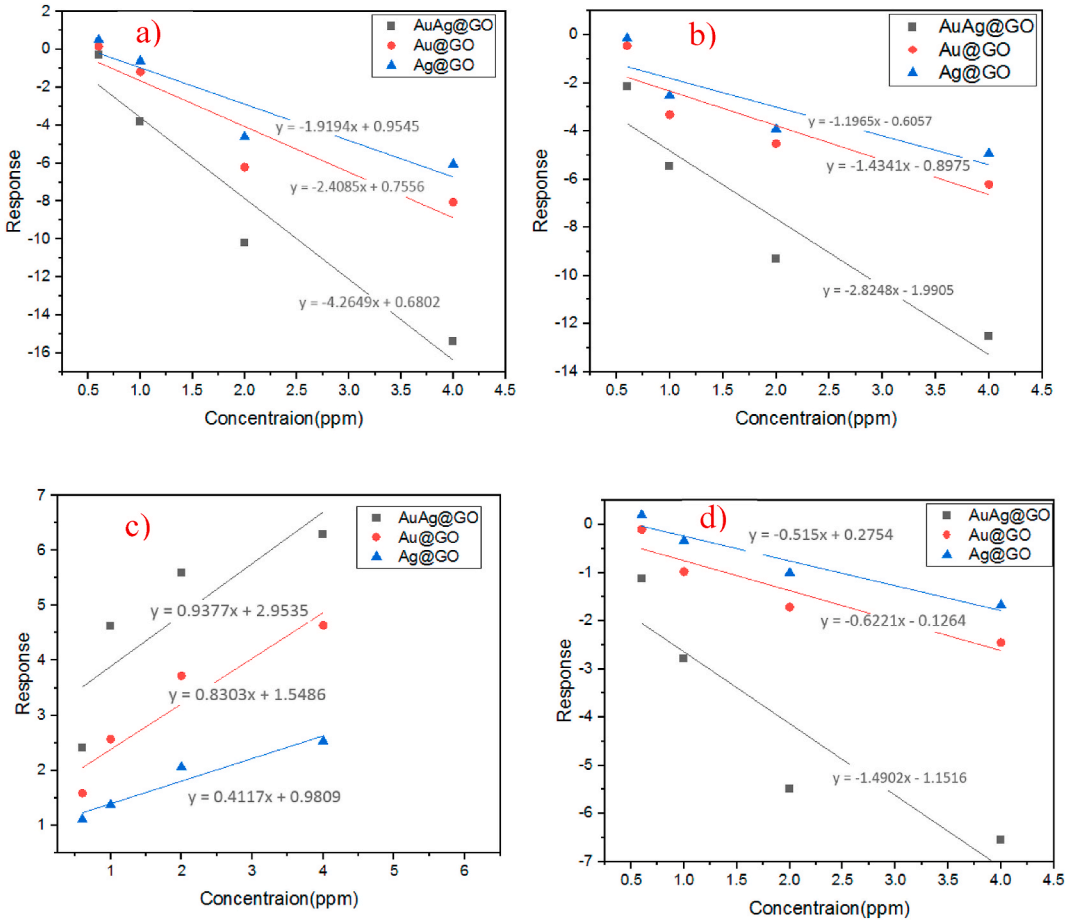

Fig. 11. Calibration curves of the Au_{20}@GO/PANI, Ag_{10}@GO/PANI and $Au_{15}Ag_{15}$@GO/PANI nanocomposite gas sensors' response in contact with a) NO_2, b) H_2S, c) CO_2, and d) acetone.

influence the work reported in this paper (article entitled "**In situ synthesis of long tubular water-dispersible polyaniline with core/shell gold and silver@graphene oxide nanoparticles for gas sensor application**").

Appendix A. Supplementary data

Supplementary data to this article can be found online at https://doi.org/10.1016/j.heliyon.2024.e26662.

References

[1] Seyed Hossein Hosseini, R.A. Khalkhali, P. Noor, Study of polyaniline conducting/electroactive polymer as sensor for some agricultural phosphorus pesticides, Monatshefte für Chemie-Chemical Monthly 141 (2010) 1049–1053, https://doi.org/10.1007/s00706-010-0374-5.

[2] Sheikh Akbar, Prabir Dutta, Chonghoon Lee, High-temperature ceramic gas sensors: a review, Int. J. Appl. Ceram. Technol. 3 (4) (2006) 302–311, https://doi.org/10.1111/j.1744-7402.2006.02084.x.

[3] Eric Bescher, John D. Mackenzie, Hybrid organic-inorganic sensors, Mater. Sci. Eng. C 6 (2–3) (1998) 145–154, https://doi.org/10.1016/S0928-4931(98)00039-3.

[4] S.C. Nagaraju, Aashis S. Roy, J.B. Kumar, Koppalkar R. Anilkumar, G. Ramagopal, Humidity sensing properties of surface modified polyaniline metal oxide composites, J. Eng. 2014 (2014), https://doi.org/10.1155/2014/925020.

[5] R. Mello, I. Hümmelgen, Ohmic contacts between sulfonated polyaniline and metals, J. Solid State Electrochem. 5 (2001) 546–549, https://doi.org/10.1007/s100080000178.

[6] W.J. Feast, J. Tsibouklis, K.L. Pouwer, L. Groenendaal, E.W. Meijer, Synthesis, processing and material properties of conjugated polymers, Polymer 37 (22) (1996) 5017–5047, https://doi.org/10.1016/0032-3861(96)00439-9.

[7] Isacco Gualandi, Marta Tessarolo, Federica Mariani, Luca Possanzini, Erika Scavetta, Beatrice Fraboni, Textile chemical sensors based on conductive polymers for the analysis of sweat, Polymers 13 (6) (2021) 894, https://doi.org/10.3390/polym13060894.

[8] Utpal Rana, Kuntal Chakrabarti, Sudip Malik, Benzene tetracarboxylic acid doped polyaniline nanostructures: morphological, spectroscopic and electrical characterization, J. Mater. Chem. 22 (31) (2012) 15665–15671, https://doi.org/10.1039/C2JM33093H.

[9] Zoran D. Zujovic, Cosmin Laslau, Graham A. Bowmaker, Paul A. Kilmartin, Amy L. Webber, Steven P. Brown, Jadranka Travas-Sejdic, Role of aniline oligomeric nanosheets in the formation of polyaniline nanotubes, Macromolecules 43 (2) (2010) 662–670, https://doi.org/10.1021/ma902109r.

[10] Y.F. Huang, C.W. Lin, Introduction of methanol in the formation of polyaniline nanotubes in an acid-free aqueous solution through a self-curling process, Polymer 50 (3) (2009) 775–782, https://doi.org/10.1016/j.polymer.2008.12.016.

[11] Meixiang Wan, A template-free method towards conducting polymer nanostructures, Adv. Mater. 20 (15) (2008) 2926–2932, https://doi.org/10.1002/adma.200800466.

[12] Jiaxing Huang, Shabnam Virji, Bruce H. Weiller, Richard B. Kaner, Polyaniline nanofibers: facile synthesis and chemical sensors, J. Am. Chem. Soc. 125 (2) (2003) 314–315, https://doi.org/10.1021/ja028371y.

[13] Xinyu Zhang, Sanjeev K. Manohar, Polyaniline nanofibers: chemical synthesis using surfactants, Chem. Commun. 20 (2004) 2360–2361, https://doi.org/10.1039/B409309G.

[14] P. Anilkumar, M. Jayakannan, Divergent nanostructures from identical ingredients: unique amphiphilic micelle template for polyaniline nanofibers, tubes, rods, and spheres, Macromolecules 41 (20) (2008) 7706–7715, https://doi.org/10.1021/ma801090f.

[15] Xue Li, Shengjun Tian, Ping Yang, Dong Ha Kim, Wolfgang Knoll, One-step route to the fabrication of highly porous polyaniline nanofiber films by using PS-b-PVP diblock copolymers as templates, Langmuir 21 (21) (2005) 9393–9397, https://doi.org/10.1021/la0514009.

[16] Veronica M. Cepak, C.R. Martin, Preparation of polymeric micro-and nanostructures using a template-based deposition method, Chem. Mater. 11 (5) (1999) 1363–1367, https://doi.org/10.1021/cm9811500.

[17] Wolfgang K. Maser, Ana M. Benito, María A. Callejas, T. Seeger, M.T. Martınez, Joachim Schreiber, J. Muszynski, et al., Synthesis and characterization of new polyaniline/nanotube composites, Mater. Sci. Eng. C 23 (1–2) (2003) 87–91, https://doi.org/10.1016/S0928-4931(02)00235-7.

[18] Sk Md Moniruzzaman, Chee Yoon Yue, Synthesis of polyaniline nanotubes using the self-assembly behavior of vitamin C: a mechanistic study and application in electrochemical supercapacitors, J. Mater. Chem. A 2 (8) (2014) 2830–2838, https://doi.org/10.1039/C3TA14309K.

[19] Wei Chen, R.B. Rakhi, Husam N. Alshareef, Facile synthesis of polyaniline nanotubes using reactive oxide templates for high energy density pseudocapacitors, J. Mater. Chem. A 1 (10) (2013) 3315–3324, https://doi.org/10.1039/C3TA00499F.

[20] Donghua Zhou, Yanhai Li, Jingyu Wang, Ping Xu, Xijiang Han, Synthesis of polyaniline nanofibers with high electrical conductivity from CTAB–SDBS mixed surfactants, Mater. Lett. 65 (23–24) (2011) 3601–3604, https://doi.org/10.1016/j.matlet.2011.08.021.

[21] Jiri Kroutil, Alexandr Laposa, Vojtech Povolny, Ladislav Klimsa, Miroslav Husak, Gas sensor with different morphology of PANI layer, Sensors 23 (3) (2023) 1106, https://doi.org/10.3390/s23031106.

[22] Kuntima Pattanarat, Nattasamon Petchsang, Tanakorn Osotchan, I-Ming Tang, Yong-Hoon Kim, Rawat Jaisutti, High conductivity and durability textile gas sensor-based polyaniline-decorated-poly (3, 4-ethylenedioxythiophene)/Poly (4-styrenesulfonate) for ammonia detection, ACS Appl. Polym. Mater. 4 (12) (2022) 9006–9014, https://doi.org/10.1021/acsapm.2c01374.

[23] Clarice Steffens, Marcos L. Corazza, Elton Franceschi, Fernanda Castilhos, Paulo SP. Herrmann Jr., J. Vladimir Oliveira, Development of gas sensors coatings by polyaniline using pressurized fluid, Sensor. Actuator. B Chem. 171 (2012) 627–633, https://doi.org/10.1016/j.snb.2012.05.044.

[24] Mahdi Tohidian, Seyed Reza Ghaffarian, Mohadeseh Nouri, Elham Jaafarnia, Amir Hossein Haghighi, Polyelectrolyte nanocomposite membranes using imidazole-functionalized nanosilica for fuel cell applications, J. Macromol. Sci., Part B 54 (1) (2015) 17–31, https://doi.org/10.1080/00222348.2014.982485.

[25] Amir Hossein Haghighi, Mahdi Tohidian, Abolfazl Ghaderian, Seyed Emadodin Shakeri, Polyelectrolyte nanocomposite membranes using surface modified nanosilica for fuel cell applications, J. Macromol. Sci., Part B 56 (6) (2017) 383–394, https://doi.org/10.1080/00222348.2017.1316652.

[26] S.G. Pawar, S.L. Patil, M.A. Chougule, P.R. Godse, D.K. Bandgar, V.B. Patil, Fabrication of polyaniline/TiO2 nanocomposite ammonia vapor sensor, Journal of Nano-and Electronic Physics 3 (1) (2011) 1056.

[27] Axel Houdayer, Raphaël Schneider, Denis Billaud, Jaafar Ghanbaja, Jacques Lambert, New polyaniline/Ni (0) nanocomposites: synthesis, characterization and evaluation of their catalytic activity in Heck couplings, Synth. Met. 151 (2) (2005) 165–174, https://doi.org/10.1016/j.synthmet.2005.04.003.

[28] John M. Kinyanjui, David W. Hatchett, J. Anthony Smith, Mira Josowicz, Chemical synthesis of a polyaniline/gold composite using tetrachloroaurate, Chem. Mater. 16 (17) (2004) 3390–3398, https://doi.org/10.1021/cm049478i.

[29] Iole Venditti, Ilaria Fratoddi, Maria Vittoria Russo, Andrea Bearzotti, A nanostructured composite based on polyaniline and gold nanoparticles: synthesis and gas sensing properties, Nanotechnology 24 (15) (2013) 155503, https://doi.org/10.1088/0957-4484/24/15/155503.

[30] Shun-Jia Lin, Hong-Juan Sun, Tong-Jiang Peng, Linn-Hai Jiang, Synthesis of high-performance polyaniline/graphene oxide nanocomposites, High Perform. Polym. 26 (7) (2014) 790–797, https://doi.org/10.1177/0954008314529982.

[31] Victor Chabot, Drew Higgins, Aiping Yu, Xingcheng Xiao, Zhongwei Chen, Jiujun Zhang, A review of graphene and graphene oxide sponge: material synthesis and applications to energy and the environment, Energy Environ. Sci. 7 (5) (2014) 1564–1596, https://doi.org/10.1039/C3EE43385D.

[32] Amirhossein Hasani, Hamed Sharifi Dehsari, Milad Asghari Lafmejani, Alireza Salehi, Faramarz Afshar Taromi, Kamal Asadi, Soo Young Kim, Ammonia-sensing using a composite of graphene oxide and conducting polymer, Phys. Status Solidi Rapid Res. Lett. 12 (5) (2018) 1800037, https://doi.org/10.1002/pssr.201800037.
[33] Manoj Kumar, Smriti Sharma, Rishi Pal, Bhavna Vidhani, A novel gas sensor based on activated charcoal and polyaniline composites for selective sensing of methanol vapors, Sensor Actuator Phys. 353 (2023) 114210, https://doi.org/10.1016/j.sna.2023.114210.
[34] Aparna Singh, Pukhrambam Dipak, Asif Iqbal, Anuradha Samadhiya, Shailendra Kumar Dwivedi, Dinesh Chandra Tiwari, Rajendra Kumar Tiwari, Kailash Nath Pandey, Fast response and recovery polyaniline montmorillonite reduce graphene oxide polymer nanocomposite material for detection of hydrogen cyanide gas, Sci. Rep. 13 (1) (2023) 8074, https://doi.org/10.1038/s41598-023-32151-0.
[35] Narayan Karmakar, Shilpa Jain, Rohan Fernandes, Akshara Shah, Uday Patil, Navinchandra Shimpi, Dushyant Kothari, Enhanced sensing performance of an ammonia gas sensor based on Ag-decorated ZnO nanorods/polyaniline nanocomposite, ChemistrySelect 8 (18) (2023) e202204284, https://doi.org/10.1002/slct.202204284.
[36] Lorraine Mulfinger, Sally D. Solomon, Mozghan Bahadory, Aravindan V. Jeyarajasingam, Susan A. Rutkowsky, Charles Boritz, "Synthesis and study of silver nanoparticles.", J Chem. Educ. 84 (2) (2007) 322, https://doi.org/10.1021/ed084p322.
[37] Judith Kimling, Maryrita Maier, Berta Okenve, Vassilios Kotaidis, H. Ballot, Anton Plech, "Turkevich method for gold nanoparticle synthesis revisited.", J. Phys. Chem. B 110 (32) (2006) 15700–15707, https://doi.org/10.1021/jp061667w.
[38] Bahareh Rezaei, Faramarz Afshar-Taromi, Zahed Ahmadi, Shima Amiri Rigi, Niloofar Yousefi, Enhancement of power conversion efficiency of bulk heterojunction polymer solar cells using core/shell, Au/graphene plasmonic nanostructure, Mater. Chem. Phys. 228 (2019) 325–335, https://doi.org/10.1016/j.matchemphys.2019.02.084.
[39] S. Sathiyanarayanan, S. Muthkrishnan, G. Venkatachari, Corrosion protection of steel by polyaniline blended coating, Electrochim. Acta 51 (28) (2006) 6313–6319, https://doi.org/10.1016/j.electacta.2006.04.015.
[40] Mona H. Abdel Rehim, Ahmed M. Youssef, Heba Al-Said, Gamal Turky, Mohamad Aboaly, "Polyaniline and modified titanate nanowires layer-by-layer plastic electrode for flexible electronic device applications.", RSC Adv. 6 (97) (2016) 94556–94563, https://doi.org/10.1039/C6RA18748J.
[41] K. Gupta, P.C. Jana, A.K. Meikap, Optical and electrical transport properties of polyaniline–silver nanocomposite, Synth. Met. 160 (13–14) (2010) 1566–1573, https://doi.org/10.1016/j.synthmet.2010.05.026.
[42] Liangfei Ouyang, Qian Liu, Chaoping Xu, Changgui Liu, Heng Liang, Powder X-ray diffraction detection on a paper-based platform, Talanta 164 (2017) 283–290, https://doi.org/10.1016/j.talanta.2016.11.021.
[43] Mingjun Yang, Vasileios Koutsos, Michael Zaiser, Interactions between polymers and carbon nanotubes: a molecular dynamics study, J. Phys. Chem. B 109 (20) (2005) 10009–10014, https://doi.org/10.1021/jp0442403.
[44] Jian Chen, Haiying Liu, Wayne A. Weimer, Mathew D. Halls, David H. Waldeck, Gilbert C. Walker, Noncovalent engineering of carbon nanotube surfaces by rigid, functional conjugated polymers, J. Am. Chem. Soc. 124 (31) (2002) 9034–9035, https://doi.org/10.1021/ja026104m.
[45] Cheng-Ho Chen, Thermal studies of polyaniline doped with dodecyl benzene sulfonic acid directly prepared via aqueous dispersions, J. Polym. Res. 9 (2002) 195–200, https://doi.org/10.1023/A:102139572606.
[46] Paula CS. Faria-Tischer, Carlos AR. Costa, Izadora Tozetti, Luiz H. Dall'Antonia, Marcio Vidotti, Structure and effects of gold nanoparticles in bacterial cellulose–polyaniline conductive membranes, RSC Adv. 6 (12) (2016) 9571–9580, https://doi.org/10.1039/C5RA25332B.
[47] Hyun-Woo Park, Taejoon Kim, Jinyoung Huh, Minjeong Kang, Ji Eun Lee, Hyeonseok Yoon, Anisotropic growth control of polyaniline nanostructures and their morphology-dependent electrochemical characteristics, ACS Nano 6 (9) (2012) 7624–7633, https://doi.org/10.1021/nn3033425.
[48] Tursun Abdiryim, Xiao-Gang Zhang, Ruxangul Jamal, Comparative studies of solid-state synthesized polyaniline doped with inorganic acids, Mater. Chem. Phys. 90 (2–3) (2005) 367–372, https://doi.org/10.1016/j.matchemphys.2004.10.036.
[49] Young Moo Lee, Jae Hoon Kim, Jong Seok Kang, Seong Yong Ha, Annealing effects of dilute polyaniline/NMP solution, Macromolecules 33 (20) (2000) 7431–7439, https://doi.org/10.1021/ma992004y.
[50] G. Inzelt, M. Pineri, J.W. Schultze, M.A. Vorotyntsev, Electron and proton conducting polymers: recent developments and prospects, Electrochim. Acta 45 (15–16) (2000) 2403–2421, https://doi.org/10.1016/S0013-4686(00)00329-70.
[51] Ph Colomban, J. Tomkinson, Novel forms of hydrogen in solids: theionic'proton and thequasi-free'proton, Solid State Ionics 97 (1–4) (1997) 123–134, https://doi.org/10.1016/S0167-2738(97)00046-5.
[52] X.B. Yan, Z.J. Han, Y. Yang, B.K. Tay, NO2 gas sensing with polyaniline nanofibers synthesized by a facile aqueous/organic interfacial polymerization, Sensor. Actuator. B Chem. 123 (1) (2007) 107–113, https://doi.org/10.1016/j.snb.2006.07.031.
[53] Mahendra D. Shirsat, Mangesh A. Bangar, Marc A. Deshusses, Nosang V. Myung, Ashok Mulchandani, Polyaniline nanowires-gold nanoparticles hybrid network based chemiresistive hydrogen sulfide sensor, Appl. Phys. Lett. 94 (8) (2009), https://doi.org/10.1063/1.3070237.
[54] Zhiyang Zhang, Zhaopeng Chen, Shasha Wang, Chengli Qu, Lingxin Chen, On-site visual detection of hydrogen sulfide in air based on enhancing the stability of gold nanoparticles, ACS Appl. Mater. Interfaces 6 (9) (2014) 6300–6307, https://doi.org/10.1021/am500564w.
[55] S. Stegmeier, M. Fleischer, A. Tawil, P. Hauptmann, K. Egly, K. Rose, Mechanism of the interaction of CO2 and humidity with primary amino group systems for room temperature CO2 sensors, Procedia Chem. 1 (1) (2009) 236–239, https://doi.org/10.1016/j.proche.2009.07.059.
[56] Michael Caplow, Kinetics of carbamate formation and breakdown, J. Am. Chem. Soc. 90 (1968) 6795–6803, https://doi.org/10.1021/JA01026A041.
[57] Ladawan Ruangchuay, Anuvat Sirivat, Johannes Schwank, Electrical conductivity response of polypyrrole to acetone vapor: effect of dopant anions and interaction mechanisms, Synth. Met. 140 (1) (2004) 15–21, https://doi.org/10.1016/S0379-6779(02)01319-X.
[58] Dongzhi Zhang, Zhenling Wu, Xiaoqi Zong, Metal-organic frameworks-derived zinc oxide nanopolyhedra/S, N: graphene quantum dots/polyaniline ternary nanohybrid for high-performance acetone sensing, Sensor. Actuator. B Chem. 288 (2019) 232–242, https://doi.org/10.1016/j.snb.2019.02.093.
[59] Zeila Zanolli, Radouane Leghrib, Alexandre Felten, Jean-Jacques Pireaux, Eduard Llobet, Jean-Christophe Charlier, Gas sensing with Au-decorated carbon nanotubes, ACS Nano 5 (6) (2011) 4592–4599, https://doi.org/10.1021/nn200294h.
[60] Hao Zhang, Qun Li, Jinyu Huang, Yu Du, Shuang Chen Ruan, Reduced graphene oxide/Au nanocomposite for NO2 sensing at low operating temperature, Sensors 16 (7) (2016) 1152, https://doi.org/10.3390/s16071152.
[61] M.E. Azim-Araghi, M.J. Jafari, Electrical and gas sensing properties of polyaniline-chloroaluminium phthalocyanine composite thin films, Eur. Phys. J. Appl. Phys. 52 (1) (2010) 10402, https://doi.org/10.1051/epjap/2010133.
[62] Hanan Abdali, Bentolhoda Heli, Ajji Abdellah, Stable and sensitive amino-functionalized graphene/polyaniline nanofiber composites for room-temperature carbon dioxide sensing, RSC Adv. 9 (70) (2019) 41240–41247, https://doi.org/10.1039/C9RA06223H.
[63] Karl Crowley, "Fabrication of polyaniline-based gas sensors using piezoelectric inkjet and screen printing for the detection of hydrogen sulfide.", IEEE Sensor. J. 10 (9) (2010) 1419–1426, https://doi.org/10.1109/JSEN.2010.2044996.